

THE PRESENT WORK WAS SUBMITTED TO THE DEPARTMENT OF CONTINUUM
MECHANICS

RHEINISCH-WESTFÄLISCHE TECHNISCHE HOCHSCHULE AACHEN
FACULTY OF MECHANICAL ENGINEERING

MASTER THESIS

NONLINEAR MATERIAL PARAMETER IDENTIFICATION OF SOFT MATERIALS BASED ON AN INVERSE FINITE ELEMENT METHOD APPROACH

Presented by:	Nadia Pinedo Oruna, B.Sc.
Study programme:	General Mechanical Engineering M.Sc.
Matriculation number:	397 011
Reviewer:	Univ.-Prof. Dr.-Ing. Mikhail Itskov
Supervisor:	Rasul Abdulsalamov, M.Sc.
External supervisor:	Prof. Kazumi Matsui

Declaration of Authorship

I declare that this work has been composed by myself, and describes my own work, unless otherwise acknowledged in the text.

All sentences or passages quoted in this paper from other people's work have been specifically acknowledged by clear cross-referencing to author, work and page(s). Any photos and illustrations which are not the work of the author have been used with the explicit permission of the originator and are specifically acknowledged.

This work has not been and will not be submitted for any other degree or the obtaining of ECTS points at the RWTH Aachen University or any other institution of higher education.

Aachen, 26th of May 2023

Nadia Pinedo Oruna, B.Sc.

Contents

1	Introduction	1
1.1	Background and Problem Statement	1
1.2	Objective and Scope of the Study	1
1.3	State of the Art	2
1.3.1	Experimental Characterization for Soft Materials	2
1.3.2	Material Modeling of Soft Materials	9
1.3.3	Inverse Finite Element Method for Parameter Identification	15
1.4	Overview	17
2	Experimental Model	19
2.1	Experimental Model I	20
2.2	Experimental Model II	22
2.3	Experimental Tests Description	24
2.4	Analysis and Overview of the Data and Results	26
2.4.1	Middle Point	27
2.4.2	Load-Unloading	29
2.4.3	Nearby Point	31
2.5	Main Assumptions for Material Modeling	32
2.5.1	Level 1: Linear Elasticity	33
2.5.2	Level 2: Hyperelasticity	34
3	Computational model	35
3.1	Computational model I	35
3.1.1	Middle Point	35
3.1.2	Nearby Point	38
3.2	Analysis and Complications	39
3.2.1	Verification of the Computational Model	39
3.3	Computational model II	40
3.3.1	Middle Point	40
4	Inverse Finite Element Method for Material Parameter Identification	45
4.1	Response Surface Optimization	45
4.2	Minimizing the Objective Function	49
4.3	Comparison between RSO and MATLAB Optimization	51
5	Results	53
5.1	Overview and Analysis	53
5.2	Validation of Computational Model	55
5.2.1	Deeper Indentation	56
5.2.2	Deformation Profile Analysis	57
5.2.3	Nearby Point - Blue Point	58
5.3	Framework Proposal	65
5.4	Limitations and Implications of the Results	67

6 Conclusion and Outlook	69
6.1 Summary and Contributions	69
6.2 Recommendations for Future Research	69
6.3 Conclusions and Final Remarks	69
A Appendix	71
A.1 Experimental Research from YNU	71
Bibliography	79

List of Figures

1.1	Uniaxial tensile testing of ether-based polyurethane	3
1.2	Uniaxial compression testing setup	5
1.3	Uniaxial compression testing methodologies	6
1.4	Nanoindentation experiment diagram	7
1.5	Indentation setup of synthetic and biological tissues	8
1.6	Aspiration experiment	9
2.1	Experimental model I	20
2.2	Specimen dimensions	21
2.3	Experimental model II	23
2.4	Experimental model II diagram	23
2.5	Middle point test position	24
2.6	Load-Unloading test	25
2.7	Nearby point test positions	26
2.8	Middle Point experimental data	28
2.9	Middle Point experimental data	28
2.10	Load-Unload experimental data	29
2.11	Load-Unload Use Case: Analysis of Viscoelasticity	30
2.12	Experimental data for Middle Point vs. Nearby Point	31
2.13	Nearby Point Use Case: Shear stresses analysis	32
3.1	Computational model I geometry	36
3.2	Computational model I mesh	36
3.3	Computational model I vs. Experimental data - Linear elasticity	37
3.4	Computational model I vs. Experimental data - Neo-Hookean	38
3.5	Nearby Point: CM I vs. Experimental data - Neo-Hookean	39
3.6	Mesh convergence model I	40
3.7	Mesh convergence model I stress distribution	41
3.8	Computational model II mesh	42
3.9	Stress distribution analysis	43
3.10	CP II: No platform vs. with platform	44
4.1	Local sensitivity analysis - Initial parameter range	47
4.2	Response surface - Force Reaction	47
4.3	Multi-objective optimization comparison	49
4.4	Polynomial approximation surfaces-NRMSE	50
4.5	Polynomial approximation surfaces-MRE	50
5.1	Best material parameter sets load-displacement curves	55
5.2	Deeper Indentation - Stress distribution	56
5.3	First validation case load-displacement curves	57
5.4	Deformation profile - Diagram	58
5.5	Deformation profile experiment	59

5.6	Deformation profile - Computational model	60
5.7	Second validation case measurement data	60
5.8	Blue point - Diagram	61
5.9	Blue point computational model	62
5.10	Middle point force components comparison	63
5.11	Blue point force components comparison	64
5.12	Framework proposal	66
A.1	Experimental device	73
A.2	Simulated organ	73
A.3	Schematic diagram YNU	74
A.4	Time history of trigger voltage	75
A.5	Specifications of miniature 6-axis force sensors	75
A.6	Deformation measurement	76
A.7	Reaction force components results	77
A.8	Deformation results	77

List of Tables

4.1	Material parameter sets obtained from MATLAB	50
5.1	Best material parameter sets	54
5.2	Goodness of fit	55
5.3	NRMSE for first validation case	57
5.4	NRMSE for second validation case	58
5.5	Force components NRMSE	62

List of Abbreviations

FEA	Finite Element Analysis
FEM	Finite Element Method
iFEM	inverse Finite Element Method
ASME	(The) American Society (of) Mechanical Engineering
TSSA	Transparent Structural Silicone Adhesive
PDMS	PolyDiMethylSiloxane
MAS	Minimal Access Surgery
FE	Finite Element
NH	Neo-Hookean
MR	Mooney-Rivlin
YM	Yeoh Model
OM	Ogden Model
RMSE	Root Mean Square Error
EM I	Experimental Model I
EM II	Experimental Model II
MP	Middle Point
LU	Load Unloading (Case)
NBP	Nearby Point
CM I	Computational Model I
CM II	Computational Model II
RSO	Response Surface Optimization
DOE	Design Of Experiments
MOGA	Multi-Objective Genetic Algorithm
FR	Full Range
RR	Reduced Range
2P	2 Point target
3P	3 Point target
NRMSE	Normalized Root Mean Square Error
MRE	Mean Relative Error
MAPE	Mean Absolute Percentage Error
RRMSE	Relative Root Mean Square Error
VC I	Validation Case I
VC II	Validation Case II
BP	Blue Point

List of Symbols

A_b	cross-sectional area of the bar	(m)
A_s	cross-sectional area of the specimen	(m)
l_s	specimen gauge length	(m)
C_b	wave speed through the bar	(m s ⁻¹)
v_{UC}	testing speed for compression test	(m s ⁻¹)
E	Young's Modulus	(N mm ⁻²)
S_{ijkl}	compliance tensor	
C_{ijkl}	stiffness tensor	
I_1^*	distortional first invariant	
I_2^*	distortional second invariant	
J	Jacobian of the deformation gradient	
b^*	left Cauchy-Green strain tensor	
I	identity matrix	
C_{10}, C_{01}	Mooney-Rivlin material parameter constants	
C_{10}, C_{20}, C_{30}	Yeoh model material parameter constants	
D_k	volumetric D-parameter	
F_s	simulated force	(N)
F_e	experimental force	(N)
n	number of data points	
r_{i1}	indenter head radius of experimental model I	(mm)
l_{i1}	indenter length of EMI	(mm)
r_1	specimen minor radius	(mm)
r_2	specimen major radius	(mm)
r_{t1}	specimen tumor minor radius	(mm)
r_{t2}	specimen tumor major radius	(mm)
r_{i2}	indenter head radius of experimental model II	(mm)
E_{i2}	Young's Modulus of indenter of EMII	(N mm ⁻²)
F_x	force reaction in X-direction of EMII	(N)
F_y	force reaction in Y-direction of EMII	(N)
F_z	force reaction in Z-direction of EMII	(N)
h_I	indentation depth of EMI	(mm)
h_{II}	indentation depth of EMII	(mm)
p_{I1}	nearby point of EMI	(mm)
p_{II1}	first nearby point of EMII	(mm)
p_{II2}	second nearby point of EMII	(mm)
p_{II3}	third nearby point of EMII	(mm)
$u_{I_{MP}}$	maximum displacement of the middle point of EMI	(mm)
$F_{I_{MP}}$	maximum force of the middle point of EMI	(N)
$u_{II_{MP}}$	maximum displacement of the middle point of EMII	
$F_{Z_{II,MP}}$	maximum force component in X-direction	(N)
$F_{Y_{II,MP}}$	maximum force component in Y-direction	(N)
$F_{X_{II,MP}}$	maximum force component in Z-direction	(N)

$F_{I_{LU}}$	force of the loading-unloading case of EMI	(N)
$F_{II_{LU}}$	force of the loading-unloading case of EMII	(N)
$F_{I_{NBP}}$	maximum force component of nearby point of EMI	(N)
$F_{II_{NB}}$	force component of the nearby point of EMII	(N)
A	contact area between specimen and indenter	(mm)
r_i	radius of the indenter	(mm)
F	applied indented force	(N)
h	indentation depth	(mm)
C_1	material constant of hyperelastic model	
D_1	material incompressibility parameter	(MPa ⁻¹)
J	determinant of the elastic deformation gradient	
I_1	first invariant of the right Cauchy-Green deformation tensor	
W	elastic strain energy potential function for the NH material	
K	initial bulk modulus	(N mm ⁻²)
e_{I_s}	global element size of the specimen's mesh CM I	(mm)
e_{I_a}	contact sizing element size for CM I	(mm)
E_{LE}	Young's modulus of the linear elastic model	(N mm ⁻²)
u	indenter's displacement	(mm)
$D_{1_{CMI}}$	incompressibility parameter for CM I	(MPa ⁻¹)
e_{M_s}	specimen's element size for mesh convergence model	(mm)
e_{M_i}	indenter's element size for mesh convergence model	(mm)
e_{M_a}	refinement's element size for mesh convergence model	(mm)
r_{M_a}	radius of refinement area for mesh convergence model	(mm)
e_{II_s}	global element size of the specimen's mesh CM II	(mm)
e_{II_i}	element size of the indenter's mesh CM II	(mm)
r_{II_a}	radius of refinement area for CM II	(mm)
h_{VC1}	indentation depth of first validation case	(mm)
$\sigma(t)$	stress	(N mm ⁻²)
$\epsilon(t)$	strain	
ϵ_t	transmitted strain signal	
ϵ_r	reflected strain signal	
ϵ_{ij}	strain tensor	
σ_{ij}	stress tensor	
ν	Poisson's ratio	
δ_{ij}	Kronecker delta function	
μ	shear modulus	(N mm ⁻²)
λ	Lame's constant	
κ	bulk modulus	(N mm ⁻²)
ψ	Helmholtz free energy per unit reference volume	
σ	Cauchy stress	
λ_i	stretches of the deformation	
α_k	alpha-parameters	
ν_{i2}	Poisson's ratio of indenter of EM II	
σ	stress of linear elastic model	(N mm ⁻²)
ϵ	strain of linear elastic model	
λ	principal stretches	
μ	shear modulus or the second Lamé parameter	(N mm ⁻²)
μ_{CMI}	shear modulus for CM I	(N mm ⁻²)

1 Introduction

1.1 Background and Problem Statement

The biomechanical characterization of soft tissues has gained attention in medical research [7], in areas such as medical image analysis and visualization. For many years, the obtained medical diagnoses were often based on the assumptions of experts or their accumulated experience. While these information have proven to be useful in general, these methods have limitations in cases where quantifiable data is necessary, specifically for computer-assisted systems, e.g., medical diagnosis, therapy, and training [18]. To gather the material data, e.g., elasticity, stiffness, response under deformation and temperature, it is required to gain access to the soft tissues and perform *in vivo* testing experiments. However, obtaining accurate biomechanical data can be challenging due to the invasive nature of the procedures and the difficulty in maintaining constant and reproducible internal or external factors in experimental configurations [4].

Especially, when it comes to internal organs, obtaining reliable data for examination after their extraction is difficult because the material properties can vary between samples or testing locations on the same organ [5]. This is due to the influence of various factors such as changes in blood pressure, changes in material properties over time, symptoms of disease, and more. In addition, another problem is the lack of replication, due to the use of different individuals' organs, which introduces more external factors into the equation. Moreover, given a tissue sample, it is difficult to properly characterize the material due to its anisotropic property, which can lead potentially to inaccuracies in the result [7].

In the situation where the material data can be collected in a constant, fast and reliable process, a material model can be established and the computer-aided systems can predict the mechanical behavior of soft tissues, providing preoperative calculations. This demonstrates the importance of material data collection and material model development, especially in the context of computational models such as engineering simulation models created finite element analysis (FEA) software and their medical applications in medical devices, surgical procedures, and training softwares [4]. By using accurate material models, the accuracy of the simulation can be improved, aiding in a better understanding and predicting a soft tissue response to external stimuli [33], making them more useful in medical research and other related applications.

1.2 Objective and Scope of the Study

Soft materials, characterized by low elastic moduli and high sensitivity to external stimuli, frequently experience large deformation and display nonlinear responses [33], making the finite element method (FEM) a common approach for analyzing

these materials and solving continuum mechanical problems. Although FEM facilitates the analysis of complex structures with complex material behavior, simulating such materials requires high computational costs.

The main objective of this study is to identify the key parameters of soft materials and their influence on the development of a material model based on inverse finite element method (iFEM) approach. By identifying these key parameters, an attempt is made to approximate the behavior of complex materials through a simplified material model and assess its potential future applications in medical research and its use with organs.

To achieve this goal, an experimental configuration will be selected, and a computational model will be developed to use an iFEM approach to identify the key material parameters of the given soft material. With this method, it was possible to match the results of the computational model to the experimental data, and validate the model with additional data points.

The objective of this study is to develop a framework that identifies the essential material parameters of soft materials and evaluates their limitations and impact on a validated model, which can describe nonlinear material behavior. By contributing to this framework, the study aims to accelerate the development of material models for practical applications in medical research and development.

1.3 State of the Art

This section reviews the state of the art relevant to this study. First, the experimental characterization techniques are reviewed, including methods for obtaining mechanical and viscoelastic properties. This is followed by the description of different approaches to describe the material model for different soft materials. Then, the iFEM, which is one method to identify material parameters from experimental data, will be explained. Finally, the standard verification and validation process used in computational solid mechanics for medical devices based on the American Society of Mechanical Engineering (ASME) guidelines will be discussed. The goal of this chapter is to provide a comprehensive overview of the current methods use in the field and the identification of limitations and gaps in the current state of knowledge.

1.3.1 Experimental Characterization for Soft Materials

Experimental testing is a key approach to obtaining information about the mechanical behavior of soft materials. In order to characterize the mechanical behavior of a test specimen, the most common method method is to mechanically load the specimen and measure the response of the force against the displacement [3]. Soft materials are commonly applied for tissue engineering applications, however, challenges arise for the design of experimental design due to their elastic modulus range (kPa) and complex mechanical properties [20].

Uniaxial Tension Testing

Uniaxial tension testing are widely employed to determine an stress-strain relationship. For uniaxial tension cases, a specimen is typically loaded by gripping the ends while applying tension, and the deformation is usually measured with a strain



FIGURE 1.1: Uniaxial tensile testing: Diagram of three tensile testing of an ether-based polyurethane elastomer specimen done with three different experiment configurations for different strain rate analysis. Diagrams are based on the experiments made by Kanyanta and Ivankovic [17].

gauge [3]. This kind of testing focuses on the central region of the specimen to evade complication arising from edge effects. A homogeneous deformation in the central region is usually expected for this kind of testing, which simplifies the boundary problem and ensures that the measurements represents valid stress-strain values. However, there are two key limitations for uniaxial testing when testing soft materials; first, it may not be suitable when complex boundary conditions arise and is not possible to control the experimental condition entirely [25]. Second, these tests are inadequate to fully characterize the anisotropic behavior of these materials [7].

In a study made by Kanyanta and Ivankovic [17], the authors investigated the behavior of an ether-based polyurethane elastomer for the creation of mock arteries. Polyurethane was ideal for this application due to its high elasticity and resilience and adaptability to various shapes and sizes. Uniaxial tensile tests on dumbbell-shaped specimens were conducted, divided into three groups based on the strain rate.

For the low strain rate tensile tests ($< 1/\text{s}$), a standard Instron machine was utilized, as illustrated in Figure 1.1a. Intermediate strain rate tensile tests (between $1/\text{s}$ and $100/\text{s}$) were performed using a drop-weight tester (Fig. 1.1b). Load measurements were recorded with a calibrated strain gauge, with the zero position established at the striker and impact plate's initial contact point. High strain rate tests ($> 100/\text{s}$) were conducted with a split Hopkinson pressure bar in tension, as shown in Figure 1.1c. A swinging pendulum generated a tensile pulse, propagating along the bar into the specimen. Utilizing the transmitted and reflected strain signals and using the classical Kolsky analysis the specimen stress

$$\sigma(t) = E \frac{A_b}{A_s} \epsilon_t(t), \quad (1.1)$$

and the strain

$$\epsilon(t) = \frac{-2C_b}{l_s} \int_0^t \epsilon_r(t) dt, \quad (1.2)$$

were calculated. Here, A_b is bar's cross-sectional area, A_s the specimen's cross-sectional area, ϵ_t refers to the transmitted strain signal, ϵ_r is the reflected strain signal, l_s is the specimen gauge length, and C_b is the wave speed through the bar. Low strain rate tests were conducted under dry-room temperature, wet-room temperature, and wet at 37°C . Intermediate and high strain rate tests were performed exclusively under dry-room temperature conditions.

Test results demonstrated that ether-based polyurethane elastomer specimens were highly sensitive to temperature and humidity, as the material softened with increased levels of these factors. Young's modulus values for the dry-room temperature setup had a Young's modulus of 7.4 MPa , decreasing to 5.3 MPa and 4.7 MPa for the wet-room temperature and wet conditions, respectively. Moreover, the polyurethane exhibited varying Young's modulus values under dry-room temperature, depending on the elastomer's composition, with values ranging from 3.6 MPa to 14.8 MPa .

The material displayed minimal strain rate dependency at low strain rates, but exhibited moderate strain rate sensitivity at intermediate and high strain rates, where the Young's modulus ranged between 8 MPa and 12 MPa . However, for strains below 20 %, the outcomes showed repeatability across all strain rates tests.

For strain rates found in arteries around $< 2/\text{s}$, the variation of the Young's modulus was insignificant and this could be assumed to be constant. This study demonstrated that it is important to measure the properties of the elastomer under similar condition to the intended application, as properties varies under different conditions.

Uniaxial Compression Testing

Compression tests are also widely utilized to determine the stress-strain response and usually involve placing the specimen in between two plates and compressing the material (Fig. 1.2). The stress-strain response derived from this kind of testing serves in determining the deformation characteristics of the material including the fatigue and fracture resistance. Uniaxial compression tests may be affected by the interface friction between the specimen and the loading plates, leading to a nonhomogeneous deformation state, e.g., barrelling [3].



FIGURE 1.2: Uniaxial compression testing: Diagram of typical compression setup and influence of interface friction on the deformed specimen shape. Illustration is based on the "Mechanics of Solid Polymers" by Bergström [3].

Drass et al. [8] conducted a uniaxial compression test, showing that the lubrication was crucial for a homogenous stress and strain distribution. The specimen tested was made from Transparent Structural Silicone Adhesive (TSSA), a rubber-like material commonly used in laminated connections within glass structures. In this study homogeneous and inhomogeneous experiments were performed, as the goal was to determine an experimental setup, which ensured a homogeneous stress and strain distributions for the identification of material parameters [8].

The specimen was compressed with perfect slippage, where the plates and the specimen were lubricated before testing to ensure a frictionless support. A constant speed of $v_{UC} = 0.174 \text{ mm/min}$ was used for this test with a saBesto HHS 5000 machine. The compression test were conducted until a strain $\epsilon = 0.6$ was reached, as the standard deviation for large compression strain ($\epsilon > 0.5$) was too large. The test presented challenges in maintaining the lubrication throughout the test, as it tended to be pressed out between the test specimen and the pressure plates, resulting in increased friction.

The results of this experiment were processed to identify hyperelastic material parameters using standard fitting routines and inverse methods. The test suggested that only stress-strain response up to a strain value of $\epsilon = 0.5$ should be considered for the identification of the TSSA material parameters, as the friction's impact can be neglected for smaller strains.

In comparison, for a biomaterials, e.g., human soft tissues, a compressive testing of cartilage was conducted by Griffin et al. [13]. This study aimed to provide a protocol where compressive and tensile properties of human soft tissues can be evaluated and characterized with minimal destruction. By understanding these material's properties and calculating the Young's elastic modulus, it would be possible to obtain a benchmark for creating suitable tissue-engineered substitutes [13].

The mechanical response of cartilage is highly dependant to the fluid's flow through the tissue. The methods for compression testing can vary with confined or unconfined specimen, and the most prevalent, indentation (Fig. 1.3). In the unconfined compression the cartilage is pressured using a non-porous plate onto a non-porous chamber, leading to a predominantly radial fluid flow. For the confined compression the sample was placed in a sealed, fluid-filled impermeable chamber and loaded with a porous plate, making the fluid flow restricted to a vertical direction. Finally, the indentation testing employed a smaller indenter applied to the sample's surface perpendicularly, ensuring uniaxial compression and minimizing

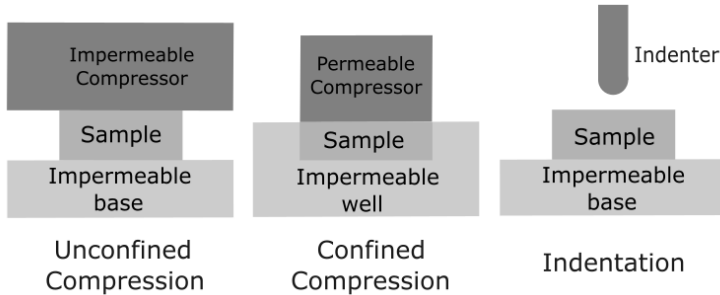


FIGURE 1.3: Uniaxial compression testing: Illustration of different compression methodologies for a cartilage specimen. Unconfined compression, confined compression and Indentation. Diagrams are based on the methodologies showed by Griffin et al. [13].

shear loading. All test were conducted in a hydrated environment and the cartilage was submerged in phosphate-buffered saline before and during the test to maintain the hydration. With the latest compression testing type it was possible to identify elastic and viscoelastic properties of the sample [13].

Indentation

Indentation testing, including micro and nanoindentation, is a popular method for characterizing the mechanical properties of soft materials [31]. One of the main advantages of indentation testing is that it requires minimal sample preparation and it is often a nondestructive technique, which allows the preservation of the geometry and tissue's architecture [26]. Furthermore, indentation is useful where more traditional testing techniques such as uniaxial or biaxial testing, are not possible to employ, and can also be utilized to evaluate nonlinear properties, e.g., viscoplastic responses[3].

Despite these advantages, there are challenges when using indentation to characterize soft materials. First, a stress-strain response is difficult to obtain due to the complex boundary conditions, which introduces an inverse problem for the identification of material parameters [26]. Second, many of the current indentation configurations assume material isotropy, which may not be the case for biomaterials [9]. In addition, determining the mechanical properties of soft materials locally or at small scales is still difficult to achieve [33].

The usual indentation testing setup is shown in Figure 1.4, in this case a system applies a certain force to an attached indenter rod where and specific indenter tip. After the indenter tip goes to a determined displacement, it is possible to obtain a load-displacement curve. The deformation can be measured through an capacitance gauge or also optically, via laser measurements [3].

In a study made by Zhang et al. [33] an investigation of spherical indentation on hyperelastic soft materials was conducted. The material utilized in the experiments was polydimethylsiloxane (PDMS), with was prepared and cured in a cylindrical mold and cured at 60 °C for eight hours. The ElectroForce 3100 was used to measuring the mechanical properties of PDMS for tensile and indentation tests. Tensile tests were performed to identify the initial shear modulus and locking stretch and their results compared with the indentation tests [33]. For the indentation tests an



FIGURE 1.4: Nanoindentation experiment setup diagram with an indenter tip attached to a rod and a polymer as specimen. Diagram is based on the "Mechanics of Solid Polymers" by Bergström [3].

spherical indenter with a 3 mm radius with a similar configuration shown in Figure 1.4 was used. The measurements were done under room temperature and a humidity of 50 % with a loading rate of 2 mm/s and a indentation depth of 3 mm. Six measurements were carried out at different locations on the specimen, generating an indentation load-displacement curves. Moreover, the initial shear modulus was determined using fitted results of the load-depth curves to the Hertzian and hyperelastic solution developed in the study.

The results exhibited that the determination of the initial shear modulus was possible but a certain depth dependence could be observed. However, a locking stretch could not be analyze due to the sensitivity of these parameters to experimental data noise [33].

For an application with biological tissues Carter et al. [4] performed indentation experiments on human and porcine organs for its application in realistic computer-based simulators for minimal access surgery (MAS) training. This study investigated the stress-strain data of the pig spleen and liver for *ex vivo* experiments, along with human liver for *in vivo* experiments from volunteers patients undergoing a minor surgery. For the *ex vivo* experiment a static indentation setup was used as shown in Figure 1.5a, where the specimens were placed on a flat surface. A force was applied manually with a winding mechanism at constant rate of 1 mm/s with a rounded indenter with a diameter of 4.5 mm. Ten measurements were carried out on each tissue sample and the load-displacement measurements were gathered with a computerized system with a sampling rate of 15 Hz.

The *in vivo* experiments were carried out using a hand-held compliance probe. To achieve an overall consistency of the measurements the same surgeon performed the experiments. In addition to maintain consistent indentation depth of 5 mm the indenter was surrounded with a reference ring to provide stability in the measurements (Fig. 1.5b). The force exerted by the weight of the ring was around 0.5 N, while the friction force between the ring and the surface tissue was below 0.05 N,

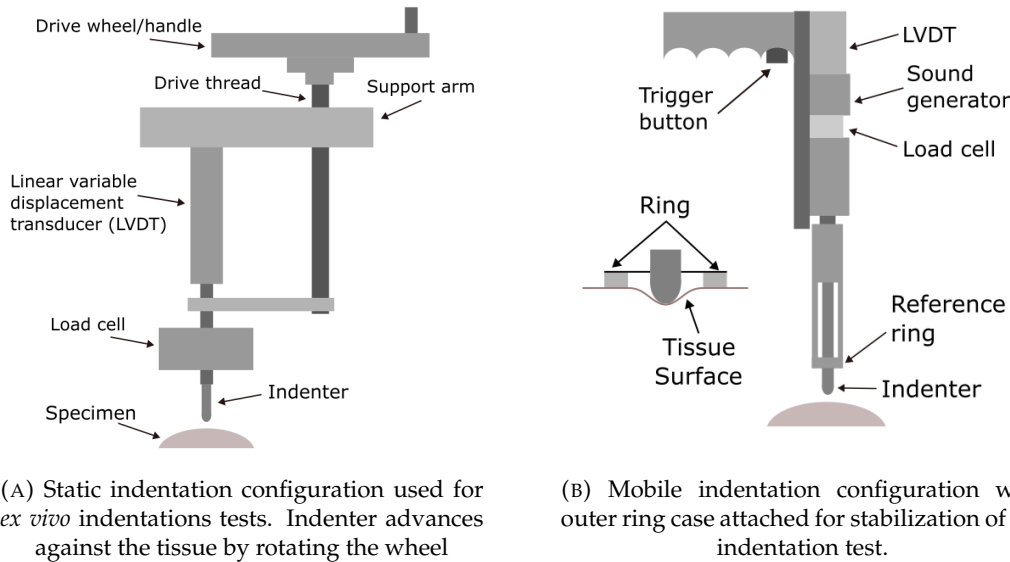


FIGURE 1.5: Indentation testing: Diagram of static and mobile indentation tests, indenters were attached to a load cell, which was connected to a displacement transducer. Diagrams are based on the study made by Carter et al. [4].

making it a negligible effect [4]. The probe was positioned on the tissue and the desired indentation depth was indicated with an audible signal. The indentation rate for this configuration ranged from 3 mm/s to 4 mm/s and six measurements were carried out on each patient.

The results were analyzed using MATLAB and showed highly nonlinear stress-strain behavior and large variances. For the reduction of these variances due to the inhomogeneity of the materials and changes over time, the average of the repeated measured was calculated. The measured elastic moduli of pig spleen and liver was 0.11 MPa and 4 MPa respectively, and for the human liver about 0.27 MPa was measured. However, a diseased liver showed a higher elastic modulus of 0.74 MPa [4].

Aspiration Experiment

Tissue aspiration experiments were a method introduced by Kauer et al. [18] for determining the material parameters of biological soft tissues *in vivo*. In this study the method was validated with a synthetic material, silgel, a very soft gel-like material with similar properties to biological soft tissues. This material was ideal to use it for the validation of the aspiration method before applying it to human tissues [18].

The biological soft tissue used in this paper was human uterus. This tissue was selected because it possesses a complex, multilayered structure with anisotropic properties. Moreover, hysterectomy (removal of the uterus) is common surgical procedure, which provides a good chance to perform measurements before and after the removal of the organ.

This method introduced an aspiration tube which is put against the soft tissue, generating a vacuum causing the deformation of the tissue (Fig. 1.6). An advantageous feature of this experimental technique is that it can be performed *in vivo* and *ex vivo*. With the help of a mirror placed next to aspiration hole, the reflection of the side-view of the tissue can be captured with a video camera. This camera captures

the images of the illuminated surface of the material and the aspiration pressure is captured through a sensor. Through this process the captured profile of the tissue is obtained and this can be used to characterize the deformation and analyze the viscoelastic properties of the soft tissue [18].

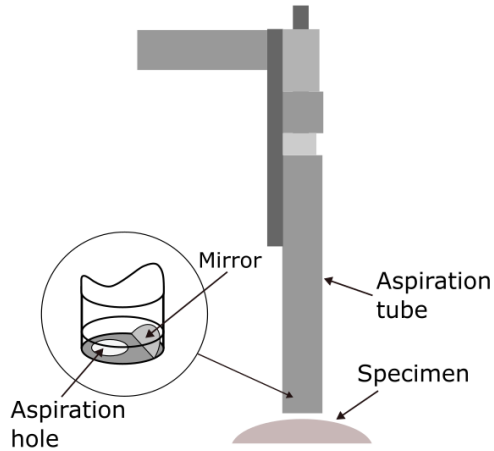


FIGURE 1.6: Aspiration experiment setup: Diagram showing aspiration tissue vertically positioned to the target tissue, inside of the tube a mirror reflects the side view of the tissue to the video camera on top. Diagram based on the research of Kauer et al. [18].

The main benefits in comparison to more traditional experimental techniques are, the well-defined mechanical boundary conditions during the experiment's execution, the assessment of large deformation experiments, and the analysis of the viscoelastic properties of the tissue for real surgical procedures due to the time dependent resolution of the deformation.

The results from these experiments corroborates that the development of experimental designs for biological soft tissues and its application in real-world scenarios are essential to understand their mechanical behavior and make advance in medical research.

1.3.2 Material Modeling of Soft Materials

Material models, such as linear elasticity and hyperelasticity play a crucial role for the characterization of material properties, as these describe a relationship that represents how a material behaves, e.g, the stress response for an applied strain, or the heat transfer for a defined temperature gradient. For the case of soft materials, hyperelastic models are usually useful candidates, as these models can often predict the behavior of complex materials under certain limitations. Moreover, hyperelastic models can be used as a foundation for more advance models like viscoelastic and viscoplastic models [3].

Hyperelastic models are useful due to their ease of use and calibration, accessibility in major commercial FE softwares, and computational efficiency. While these models are accurate for monotonic loading, these models possess some limitations, such as not capturing rate effects, i.e., viscoelasticity, or hysteresis during cyclic loading [3].

In this subsection, linear elasticity and hyperelasticity constitutive models will be presented based on the overview made by Bergström [3], followed by examples

from the research papers from the Subsection 1.3.1 to confirm the relevance of these models for medical research.

Linear Elasticity

This model is the most basic approach to represent the small strain of the mechanical behavior of solid polymers, with isotropic elasticity being its most elementary form [3]. In isotropic elasticity, stress is proportional to the applied strain and independent of the material's orientation. Hooke's law is frequently the constitutive equation for an elastic material, and one form

$$\epsilon_{ij} = \frac{1 + \nu}{E} \sigma_{ij} - \frac{\nu}{E} \sigma_{kk} \delta_{ij}, \quad (1.3)$$

was presented by Bergström [3] to define a strain-stress relationship, where the indices i and j take the values of 1, 2, and 3, ϵ_{ij} and σ_{ij} are the strain and stress tensors, and

$$\delta_{ij} = \begin{cases} 1, & \text{if } i = j, \\ 0, & \text{otherwise,} \end{cases} \quad (1.4)$$

represents the Kronecker delta function. Similarly, the stress

$$\sigma_{ij} = 2\mu\epsilon_{ij} + \lambda\epsilon_{kk}\delta_{ij}, \quad (1.5)$$

can be determined in terms of the strain using Hooke's Law. Key parameters in Equations 1.3 and 1.5 include the Young's Modulus E , Poisson's ratio ν , the shear modulus μ , and the Lame's constant λ . The linear elastic constitutive theory can be formulated with the identification of two material parameters, which can be determined through experimental data. After identifying these two parameters, it is possible to calculate any other constants. A typical experimental method to identify and calibrate a pair of parameters is the uniaxial tension test, where the stress-strain response identifies E and ν . A significant drawback of using a linear elastic model to predict the mechanical behavior of soft polymers is that these materials exhibit linear behavior only within small strains and a limited range of strain-rates and temperatures [3].

Anisotropic Elasticity

Anisotropic elasticity is an extension of linear elasticity theory that considers the anisotropic behavior of the material, as is usually the case for biopolymers. The strain ϵ_{ij} and stress σ_{ij}

$$\epsilon_{ij} = S_{ijkl}\sigma_{kl}, \quad (1.6)$$

$$\sigma_{ij} = C_{ijkl}\epsilon_{kl}, \quad (1.7)$$

can be written using Hooke's Law for an anisotropic material. These equations show that the stress and strain tensor are linearly dependent on each other by a linear stiffness C_{ijkl} or compliance tensor S_{ijkl} . The stiffness and compliance tensors possess 81 components and since the stress and strain tensors are symmetrical, the independent components of S and C can be then reduced to 36 components. Depending on the degree of anisotropy, these matrices can be further simplified.

Hyperelasticity

Hyperelastic models are an extension of linear elasticity that accounts for nonlinearity and large strain predictions. These models have been widely developed over the years and are available in various FE softwares. Hyperelastic models are very important in modeling soft tissues, as they can be sometimes connected to the micromechanisms driving the deformation behavior of the material [3]. Common hyperelastic models include the Neo-Hookean, Mooney-Rivlin and Ogden models.

Neo-Hookean Model

The Neo-Hookean (NH) model consists of a simple hyperelastic model based on the shear modulus μ and the bulk modulus κ . This model can be used for compressible and incompressible deformations, with the compressible version often being more practical for finite element simulations. The NH model is primarily used for solid, rubber-like materials characterized by an almost incompressible behavior. Because of this characteristic, the actual value has a minimal effect on the response of the observed material [3].

The NH model is like other hyperelastic models, specified by its Helmholtz free energy per unit reference volume

$$\psi(I_1^*, J) = \frac{\mu}{2}(I_1^* - 3) + \frac{\kappa}{2}(J - 1)^2, \quad (1.8)$$

where I_1^* is the distortional first invariant, and J the Jacobian of the deformation gradient [32]. This equation is inadequate for the accurate description of large-strain nonlinear responses. In addition, this equation is not dependent on the second invariant I_2^* , which limits the stress prediction for biaxial loading.

The Cauchy stress for compressible NH model can be expressed as [32]

$$\sigma = \frac{\mu}{J} \text{dev}[\mathbf{b}^*] + \kappa(J - 1)\mathbf{I}, \quad (1.9)$$

where \mathbf{b}^* is the left Cauchy-Green strain tensor, and \mathbf{I} is the identity matrix. The Cauchy stress expressions for uniaxial, planar and biaxial deformations for incompressible NH models are

$$\sigma_{\text{uniax}} = \mu(\lambda^2 - 1/\lambda), \quad (1.10)$$

$$\sigma_{\text{planar}} = \mu(\lambda^2 - 1/\lambda^2), \quad (1.11)$$

$$\sigma_{\text{biaxial}} = \mu(\lambda^2 - 1/\lambda^4), \quad (1.12)$$

respectively. In these equations, λ represents the stretches of the deformation [32]. An alternative formulation of the NH model, where the stress is not divided into deviatoric and volumetric parts, is given by

$$\sigma = \frac{\mu}{J}(\mathbf{b} - \mathbf{I}) + \kappa(J - 1)\mathbf{I}. \quad (1.13)$$

The predictions from the standard NH model (Eq. 1.9) and this alternative formulation (Eq. 1.13) diverges with the decrease in the bulk modulus. The main advantage NH model lies in its simplicity; with the shear modulus known, the response of almost any loading mode can be determined in a robust, and computationally efficient way. However, the limitations of the model lies in capturing large-strains or when

the loading is primarily biaxial [3].

The Neo-Hookean model has been employed in various research papers to characterize soft tissue behavior. For instance, in a study from Kanyanta and Ivankovic (2010) used and compared different hyperelastic models to characterize different loading of an ether-based polyurethane (see Subsection 1.3.1). Here the elastomer was assumed to be an isotropic, incompressible material for the description of the behavior of polyurethane [17].

Furthermore, Chai et al. (2013) utilized the Neo-Hookean model to calculate the Young's modulus of human carotid plaques assuming an isotropic, incompressible model. This knowledge contributes to the identification of local biomechanical properties of atherosclerotic plaque tissue for more reliable rupture risk prediction [5].

In another study made by Shi et al. (2019), a compressible NH model was used to describe the ground substance of the fiber network of the cervical stroma. Using this model it was possible to identify the μ and λ and then calculate the Young's modulus and Poisson's ratio [26].

Mooney-Rivlin

The Mooney-Rivlin (MR) model builds upon the NH model by incorporating a linear dependence on the second invariant I_2^* in the Helmholtz free energy per unit reference volume equation

$$\psi(C_{10}, C_{01}, \kappa) = C_{10}(I_1^* - 3) + C_{01}(I_2^* - 3) + \frac{\kappa}{2}(J - 1)^2, \quad (1.14)$$

where C_{10} , C_{01} , κ are the necessary material parameters for the compressible MR model [3]. These parameters are defined based on the experimental data and for small strains, the shear modulus can be represented as [32]

$$\mu = C_{10} + C_{01}. \quad (1.15)$$

The Cauchy stress for the MR model can be expressed as

$$\sigma = \frac{2}{J}(C_{10} + C_{01}I_1^*)\mathbf{b}^* - \frac{2C_{01}}{J}(\mathbf{b}^*)^2 + [\kappa(J - 1) - \frac{2I_1^*C_{10}}{3J} - \frac{4I_2^*C_{01}}{3J}]\mathbf{I}. \quad (1.16)$$

For the incompressible version of the MR model, the Cauchy stresses in uniaxial, planar and equibiaxial deformations are

$$\sigma_{\text{uniax}} = 2(\lambda^2 - 1/\lambda)[C_{10} + C_{01}/\lambda], \quad (1.17)$$

$$\sigma_{\text{planar}} = 2(\lambda^2 - 1/\lambda^2)[C_{10} + C_{01}], \quad (1.18)$$

$$\sigma_{\text{biaxial}} = 2C_{10}(\lambda^2 - 1/\lambda^4) + 2C_{01}(\lambda^4 - 1/\lambda^2). \quad (1.19)$$

The Mooney-Rivlin model often enhances the accuracy of the predictions of the Neo-Hookean model. However, certain loading modes can cause instability in the case of a negative C_{01} term [3].

Research papers, which used the Mooney-Rivlin model, e.g., Drass et al. (2018), utilized the MR model to describe the behavior of silicone and identify the hyperelastic parameters through inverse methods. This model showed adequate results for

the fitting of four different experimental methods; uniaxial tension and compression test, biaxial tension, and shear pancake test [8].

Likewise, this model was appropriate to simulate the nonlinear properties of breast soft tissues' deformation during a leaning forward position and running movement. By identifying the breast material properties, the bra-breast contact mechanism could be analyzed [27].

Yeoh Model

The Yeoh model (YM) is another hyperelastic model that utilizes a Helmholtz free energy in a third-order polynomial in I_1^* and independent of I_2^* . This allows the model to provide more accurate predictions than the NH model, while potentially avoiding the stability issues of the MR model [3]. The Helmholtz free energy per unit reference volume for a compressible YM can be written as

$$\psi(C_{10}, C_{20}, C_{30}, \kappa) = C_{10}(I_1^* - 3) + C_{20}(I_1^* - 3)^2 + C_{30}(I_1^* - 3)^3 + \frac{\kappa}{2}(J - 1)^2, \quad (1.20)$$

where C_{10} , C_{20} , C_{30} , and κ are the material parameters to describe this model. The Cauchy stress for the YM can be derived as

$$\sigma = \frac{2}{J}(C_{10} + 2C_{20}(I_1^* - 3) + 3C_{30}(I_1^* - 3)^2)\text{dev}[\mathbf{b}^*] + \kappa(J - 1)\mathbf{I}. \quad (1.21)$$

The independence from the I_2^* term is the main motivation for the Yeoh model. Due to the difficulty of experimentally determining the dependence of this term with the Helmholtz free energy, the neglect of this term in the YM makes it easier to apply. Moreover, the hyperelastic model is Drucker stable, which is another factor that facilitates the use of this model [3]. For the incompressible version of the Yeoh model, the Cauchy stresses in uniaxial, planar, and equibiaxial deformations can be written as

$$\sigma_{\text{uniax}} = 2[C_{10} + 2C_{20}(I_1 - 3) + 3C_{30}(I_1 - 3)^2](\lambda^2 - 1/\lambda), \quad (1.22)$$

$$\sigma_{\text{planar}} = 2[C_{10} + 2C_{20}(I_1 - 3) + 3C_{30}(I_1 - 3)^2](\lambda^2 - 1/\lambda^2), \quad (1.23)$$

$$\sigma_{\text{biax}} = 2[C_{10} + 2C_{20}(I_1 - 3) + 3C_{30}(I_1 - 3)^2](\lambda^2 - 1/\lambda^4). \quad (1.24)$$

The Yeoh model has been proven to improve the prediction of the Neo-Hookean model in various loading modes, specially in large strain scenarios. Bergström also mentions, that for the identification of the material parameters C_{10} should be positive and C_{20} , and C_{30} can be calculated as

$$C_{20} \approx -0.01C_{10}, \quad (1.25)$$

$$C_{30} \approx -0.01C_{20}. \quad (1.26)$$

In the research of Kayanta and Ivankovic (2010), several constitutive models were compared for the description of polyurethane under different loading. The results of the Yeoh model showed the best fit to the variety of experimental data, however, the Neo-Hookean model showed to be adequate with small strain deformations [17]. Additionally, Łagan et al. (2017) used the Yeoh model to analyze the accuracy of model fitting to the experimental data and estimate the mechanical properties of swine skin tissue in the abdominal region under uniaxial testing [34].

Ogden Model

The Ogden model (OM) is a highly general hyperelastic model that is determined in terms of the applied principal stretches [3]. Similar to the previous models, the Helmholtz free energy per volume can be written in various ways,

$$\begin{aligned}\psi(\lambda_1^*, \lambda_2^*, \lambda_3^*) &= \sum_{k=1}^N \frac{2\mu_k}{\alpha_k^2} ((\lambda_1^*)^{\alpha_k} + (\lambda_2^*)^{\alpha_k} + (\lambda_3^*)^{\alpha_k} - 3) \\ &\quad + \sum_{k=1}^N \frac{1}{D_k} (J - 1)^{2k},\end{aligned}\tag{1.27}$$

being this equation, one of the most common for a compressible Ogden Model. Different from previously presented models, is that the volumetric response is not defined by the bulk modulus, but instead D_k parameters. In this equation $\mu_k, \alpha_k, \lambda_i^*$ are material parameters [32]. λ_i^* are the deviatoric principal stretches defined as

$$\lambda_i^* = \frac{\lambda_i}{J^{1/3}},\tag{1.28}$$

where, λ_i are the principal stretches of the left Cauchy-Green tensor [2]. In addition, the initial bulk modulus can be defined from the incompressibility parameter D_1 as

$$\kappa = \frac{2}{D_1}.\tag{1.29}$$

Equation 1.27 makes the Ogden model versatile, but can become complicated when not selecting an appropriate set of material parameters that give stable predictions for the deformation states [3]. The principal σ_i stresses can be expressed as

$$\sigma_i = \frac{2}{J} \sum_{k=1}^N \frac{\mu_k}{\alpha_k} ((\lambda_i^*)^{\alpha_k} - \frac{1}{3}[(\lambda_1^*)^{\alpha_k} + (\lambda_2^*)^{\alpha_k} + (\lambda_3^*)^{\alpha_k}]) + \sum_{k=1}^N \frac{2k}{D_k} (J - 1)^{2k-1},\tag{1.30}$$

and the stresses for incompressible OM in uniaxial, planar and biaxial loading are given by

$$\sigma_{\text{uniax}} = \sum_{k=1}^N \frac{2\mu_k}{\alpha_k} [\lambda^{\alpha_k} - (1/\sqrt{\lambda})^{\alpha_k}],\tag{1.31}$$

$$\sigma_{\text{planar}} = \sum_{k=1}^N \frac{2\mu_k}{\alpha_k} [\lambda^{\alpha_k} - (1/\lambda)^{\alpha_k}],\tag{1.32}$$

$$\sigma_{\text{biax}} = \sum_{k=1}^N \frac{2\mu_k}{\alpha_k} [\lambda^{\alpha_k} - (1/\lambda^2)^{\alpha_k}].\tag{1.33}$$

The Ogden model turns equal to the Neo-Hookean model when $N = 1$ and $\alpha_2 = 1$. Moreover, the OM often shows a better prediction than the Neo-Hookean and Mooney-Rivlin models but is not as accurate as the Yeoh model [3].

Ahanchian et al. (2017) applied the first-order Ogden model to investigate the biomechanical behavior of human skin, particularly for the plantar heel pad tissue. This research led to a deeper understanding of the transfer of the load during walking when the foot impacts the floor, and its implication in the design of shoe soles [1].

In conclusion, the material modeling of soft materials is crucial for understanding their mechanical behavior and predicting their response to different loading conditions. Hyperelastic models, such as Neo-Hookean, Mooney-Rivlin, Yeoh and Ogden models, have been widely used to characterize synthetic and biomaterials due to their direct application and capacity to describe nonlinear behavior for small and large strains. While these models have their respective advantages and limitations, they provide a basic level of understanding of complex material behavior and serve as a foundation for more advanced models. The selection of the models will depend on the specific intended use and the desired level of accuracy.

1.3.3 Inverse Finite Element Method for Parameter Identification

The inverse Finite Element Method (iFEM) has become a powerful technique and an increasingly popular approach for the identification of material parameters for both synthetic and biological materials [20]. This method involves utilizing experimental data and numerical simulations to iteratively calibrate the material parameters until the computational model matches the experimental data. Furthermore, this approach aims to predict further experimental results with a validated computational model with an optimized set of material parameters, and extract and analyze more information about the material's behavior [18]. In nonlinear cases, where the complexity of the problem increases, iFEMs are very useful [14].

The general iFEM process can be divided into the following steps:

1. **Experimental data collection:** Experimental data of the observed material is gathered from the conducted mechanical tests, e.g., uniaxial tensile and compression testing, indentation, etc. This data, often given as a load-displacement curve, this result is the basis for the identification of the parameters [25].
2. **Finite element model development:** A finite element model is developed, which includes the definition of the geometry design, contact definition, boundary conditions and the selection of the appropriate material model [15].
3. **Initial parameter estimation:** Based on literature, experimental observations, or expert knowledge, initial estimates for the material parameters are chosen and input in the computational model [6].
4. **Optimization of the parameters:** With an optimization algorithm, the material parameters are iteratively calculated until the simulated response matches or reaches a good agreement with the experimental response. The Levenberg-Marquardt and the genetic algorithm are common algorithms employed in this step [18].
5. **Validation of the parameters:** The identified material parameters are validated by comparing the computational model predictions with the validation experimental data, which was not used in the optimization process [25].

The main strengths of the iFEM is that this method allows the identification of parameters which are difficult to obtain through conventional methods and conserves the native geometry of the specimen. Furthermore, it is particularly advantageous for the solution and quantification of nonlinear problems with complex boundary

conditions. A wide range of materials, including soft polymers and biological tissues can be analyzed, and this method allows the assumption of a homogeneous material, which helps in the description of local stresses and strain fields [25].

On the other hand, iFEM presents several limitations and challenges, this includes the need for precise and dependable data, the potential for non-unique solutions in cases of poorly defined optimization, and the inability to find a unique set of parameters to describe all heterogeneous material regions. Also, iFEM with complex boundary conditions, often demands significant computational resources and requires a sturdy optimization algorithm [10].

Synthetic Soft Materials

Synthetic soft materials are commonly used to validate inverse parameter identification processes. They exhibit similar mechanical behavior to biomaterials, allowing researchers to validate the proposed inverse finite element approach before applying it to more challenging biomaterials, where *in vivo* measurements are required.

For example, as mentioned in Subsection 1.3.1 silgel was used to validate an inverse finite element method for characterizing the tissue of human uteri. The aspiration method was used for the experimental data collection, and the FE model of the deformation of the tissue on the aspirated area, required the contact between the tube and the tissue was treated as sticking. The strain energy function

$$\bar{W} = \left(\sum_{k=1}^N \mu_i (J_1 - 3)^i \right) + \frac{1}{2} \kappa (J_3 - 1)^2, \quad (1.34)$$

was selected for the explicit displacement-pressure finite element formulations [28]. This function depends on the reduced invariants J_1, J_2, J_3 of the right Cauchy-Green deformation tensor C , and μ_i and κ are the target material parameters. For $N = 1$ a nearly incompressible Neo-Hookean model is formulated, which was chosen for the case of silgel. The Levenberg-Marquardt optimization method was selected for the optimization of three parameters: the shear moduli, and the bulk modulus. This method did not guarantee obtaining a global minimum, however after the selection of arbitrarily initial parameters, the objective function was minimized. With the set of parameters, the prediction of the tensile behavior was assessed with actual tensile tests. The prediction of the synthetic tissue demonstrated good prediction quality for these parameters [18].

Biomaterials

Ahanchian (2017) characterized the behavior of heel pad sub-layers utilizing the inverse finite element method. With the aid of the ultrasound imaging and the indentation of the plantar heel pad tissue force-strain responses were recollected for the computational model. The contact between the indentation plate and the heel skin was set frictionless, and the first-order Ogden model was chosen for the description of the heel pad behavior. The Ogden strain energy function is

$$W = \frac{\mu}{\alpha} ((\lambda_1)^\alpha + (\lambda_2)^\alpha + (\lambda_3)^\alpha - 3), \quad (1.35)$$

where λ_i are the principal stretches, μ the shear modulus, and α the deviatoric exponent, being the last two the hyperelastic material parameters. The indentation of the human heel was modeled to simulate the sub-layers of the human skin and the compression response of the material. The root mean square error

$$\text{RMSE} = \sqrt{\frac{\sum_{k=1}^N (F_s - F_e)^2}{n}}, \quad (1.36)$$

where, F_s and F_e are the simulated and experimental forces, respectively. The RMSE was the objective function to be minimized, and this process was done manually after each adjustment was input in the FE model. For the validation of μ and α parameters, magnetic resonance imaging (MRI) was utilized. A good agreement was achieved for the hyperelastic model between the simulations and the validation experiments. With this validated model a second stage was performed with a viscoelastic material model to improve the material model of heel skin sub-layers [1].

In conclusion, integrating the iFEM with the experimental techniques and material models as presented in the previous sections, researchers can effectively identify material parameters for several synthetic and biological soft materials. This approach enables the development of accurate computational models that can be used to understand complex material behavior.

1.4 Overview

The thesis is organized into six chapters, providing an in-depth analysis of experimental models, computational models, parameter identification, optimization, and validation.

Chapter 2 details the experimental models used for the inverse finite element method. Indentation experiments were performed, and the experimental points are described. The chapter also outlines the main assumptions established for the development of the material model used in the FE model.

Chapter 3 focuses on the computational model, where the FE model is thoroughly described. Furthermore, the challenges encountered in the simulation process are also discussed, providing insights into the contact problem between the indenter and the material.

Chapter 4 describes the inverse finite element method, explaining the process of material parameter identification. This chapter also describes the optimization methods explored, highlighting their importance in determining the best-fit material parameters for the experimental data.

Chapter 5 presents the discussion of a proposed framework to develop a material model with iFEM approach and the results obtained from the iFEM, and the validation of the best material parameters are presented. This chapter assesses the accuracy of the identified parameters by comparing it with other validation experiments.

Finally, **Chapter 6** concludes the thesis by summarizing the main findings, discussing the implications of the results, and providing an outlook on future research directions and potential applications in further projects.

2 Experimental Model

The first phase of this project was to design and select an appropriate experimental model. This was essential to gather the necessary data from the tested material. This data will be used to determine the design parameters that can help to characterize the material's mechanical behavior.

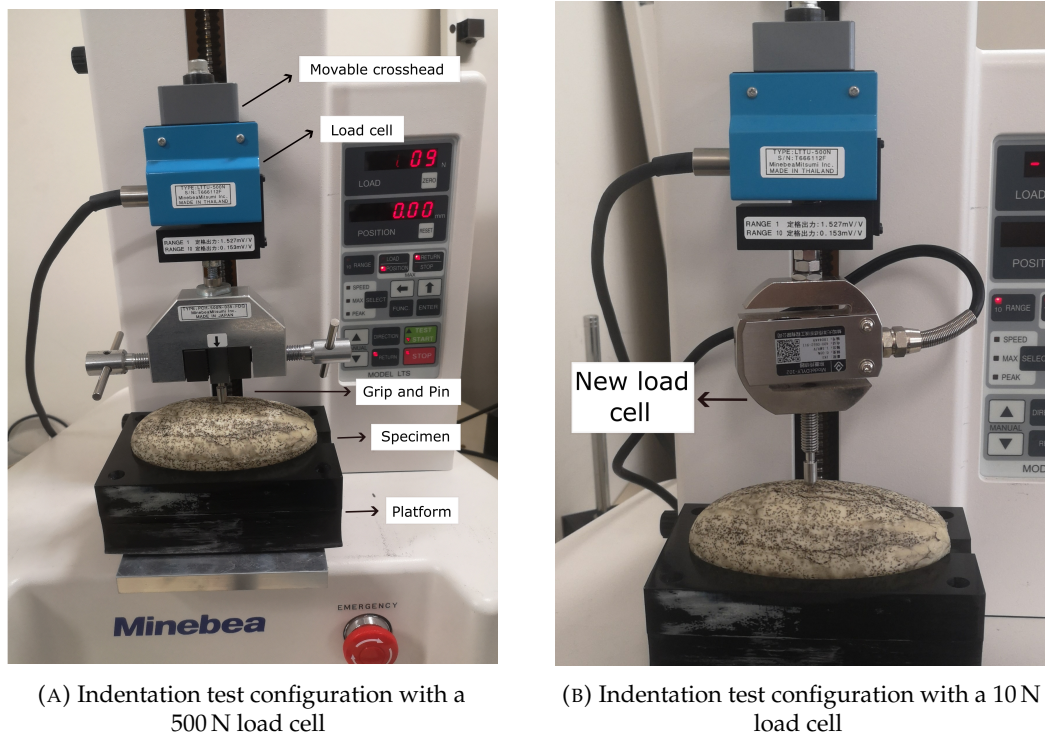
The experimental model I had the purpose of serving as a comparator for the experimental model II (see Section 2.2). The experimental model designated for analysis at the project's inception was the second model, which was developed and designed by Yokohama National University (YNU). As this second experimental model was still undergoing some improvements and corrections, a similar experiment was designed which could fulfill the same purpose.

The chosen experimental characterization for the inverse finite element method for the identification of material parameters for this project was indentation. The goal of these experiments was to observe the mechanical behavior of a soft material under compression using a rounded indenter. The aim was to determine the material behavior and observe the response under an indentation larger than the indenter radius. Additionally, by performing the indentation tests, the obtained data helped for a more in-depth understanding of the material's mechanical behavior for the chosen use cases and the determination of the main assumptions for the material modeling. The main advantage of indentation is the noninvasive feature, which is useful when a test sample should not be modified, e.g., an organ.

For both experimental setups, the specimen, which was tested, was made from a human skin gel. The human skin gel material was a two-component ultra-soft urethane resin. Polyurethane is widely used for biomedical applications, e.g., preparation of implants, wound dressings, artificial organs, and medical supplies.

Polyurethane can also be used for simulating organ tissues, as it can be tailored to mimic and match the mechanical properties of the desired biological tissues [29]. Furthermore, polyurethane can be synthesized to have a wide range of stiffness, elasticity, viscoelasticity, and can also be prepared with complex shapes for medical research purposes [16].

In this chapter, the different experimental models, which were used to evaluate the mechanical behavior of the ultra-soft polyurethane, will be described. The first two subsections, will focus on the description and procedure of the experimental models, followed by explanation of the indentation test types. Consequently, an evaluation and analysis of the results will be provided and the main assumptions for the design of the material modeling will be defined.



(A) Indentation test configuration with a 500 N load cell

(B) Indentation test configuration with a 10 N load cell

FIGURE 2.1: First experimental model: Tensile and compression machine with an indenter with a rounded head. Test Specimen made from ultra-soft polyurethane resin positioned on a fixed platform with a similar shape for constraint.

2.1 Experimental Model I

Description of the Experimental Setup

The first indentation test configuration was done by adapting a tensile and compression testing machine, model LTS - 500 NB from MinebeaMitumi.Inc (Fig. 2.1). This machine possess a maximum load capacity of 500 N, and test speeds of 10 mm/min, 20 mm/min, 30 mm/min, 50 mm/min, 75 mm/min and 100 mm/min. To achieve an indentation testing configuration, a pin was attached to the movable crosshead holding grip, as shown in Fig 2.1a. The indenter had a rounded head made of stainless steel with a radius of $r_{i1} = 3$ mm and a length of $l_{i1} = 11$ mm.

The specimen possesses a ellipsoidal form with with a minor radius $r_1 = 35$ mm and a major radius $r_2 = 60$ mm. This specimen geometry is supposed to simulate a kidney with an extracted tumor; therefore, on the lower part of the specimen a half ellipsoid with a minor radius $r_{t1} = 10$ mm and a major radius $r_{t2} = 15$ mm was removed (Fig. 2.2). The specimen was prepared by a YNU laboratory member, by 3D printing a mold with the wanted dimensions and a ellipsoidal shape, and filling it with liquid resin. Additionally, it was left to cure for around 30 h. It is relevant to clarify, that this sample had been created months before the development of this experimental setup and had been utilized in other projects conducted from the laboratory. This available specimen was positioned on a platform fixed to the base, which suited the ellipsoidal geometry for properly constraint.



FIGURE 2.2: First experimental model: Specimen dimensions made from ultra-soft polyurethane resin for indentation test.

Procedure for Conducting the Experiment

For the indentation test after placing the specimen on the platform, the indenter was positioned slightly on the surface of the point of interest. The test was conducted with a room temperature of approximately 22 °C. To perform the test the indenter was then lowered onto the surface of the specimen at a velocity of 10 mm/min. The indentation depth was controlled by limiting the maximum depth, and the test stopped once the inserted depth was reached. The indenter returned to its original position after reaching the maximum depth with a rate of 100 mm/min. Due to the material properties, the specimen returned to its original shape. The result of the indentation test was load-displacement data, which was recorded with a sampling rate of 63 Hz using a load cell of ± 500 N and a encoder to measure the displacement.

The measurement accuracy according to the specification of the machine, has a relative reading error of 1.0 %. The indentation test was repeated five times on the same sample to ensure and observe reliability and repeatability. Furthermore, the raw data collected from the test was processed and analyzed.

During the initial indentation test using the 500 N load cell, the collected experimental data showed noise that could affect the accuracy and reliability of the results. The noise was likely caused by sensitivity of the lead cell. The ultra-soft polyurethane material showed force readings, which were near the lower limit of the load cell's range, which adding any other external factors, results in noisy measurements. To address this issue, a load cell of 10 N was installed (Fig. 2.1b). This change improved the quality of the measurements and reduced the noise in the data. The change to the load cell had some implication to the experimental setup, such as removing the holding grip, and designing a part which could connect the indenter with the new load cell. In addition to changing the load cell, a simple filtering method was used to improve the experimental data. After applying the filter, the noise in the data was reduced, resulting in more smoother force reaction readings.

The applications of the combinations helped to improve the quality and accuracy of the data and gave important information about possible measurement errors to take into consideration for of the experimental model designed by YNU. At last, The filtered data was used for subsequent analysis and interpretation for the inverse finite element method approach for the material parameter identification.

2.2 Experimental Model II

The second experimental model was developed and designed by Yuta Mori, a member of the Yamada Laboratory from the Mechanical Engineering department of Yokohama National University. The main aim for this experimental method was to be able to identify the physical properties of organs in a state that closely resembles the *in vivo* environment. Additionally, this model sought two achieve two objectives: firstly, to develop a loading system to acquire the data required for an inverse analysis, and secondly, to establish a measurement process in case of a total nephrectomy [21].

Furthermore, for the present experimental setup a new sample was prepared using the same material as the previous one, i.e., human skin gel made from ultra-soft polyurethane resin, and following the same manufacturing process as described in Section 2.1.

The resulting data from the experimental model served for the basis of the material parameter identification for the inverse finite element method approach. The processed data obtained from this experimental model assisted in the calibration and assessment of the design parameters was employ in the validation for the computational model.

Description and Procedure of the Experimental Setup

In this experimental model (EM II), the indentation loading system gathered data of the indentation depth, reaction force and general deformation. The experimental device consists of an 6-axis force sensor, a laser displacement transducer, and 3D cameras placed in four directions to obtain the point cloud data based on the coordinate system of each camera. Fig.2.3 shows the setup of the experiment. For our project, the 6-axis force sensor and the laser displacement were mainly used. The loading system is operated by specifying the movement of the loading rod in advance, and the indentation is performed in the direction normal to the contact surface to prevent slippage (Fig. 2.4).

The specimen, same as in the first experimental model (Section 2.1), possessed the same dimensions, a minor radius $r_1 = 35$ mm and a major radius $r_2 = 60$ mm, and was made from ultra-soft polyurethane resin. Consequently, the platform is also bowl-shaped. For this experiment, the platform base was made from transparent acrylic resin to visually record the contact status of the bottom surface [21]. The maximum load capacity of the load cell is 200 N and a theoretical force resolution of 0.001 N. In addition, the resolution of the laser displacement sensor is 0.05 mm. The indenter is sphere-shaped with a radius of $r_{i2} = 3$ mm and was made from ruby with the following specifications; Young's Modulus of $E_{i2} = 440$ GPa and a Poisson's ratio of $\nu_{i2} = 0.3$ mm.

The indentation test was conducted under room temperature conditions. Also, the sample was placed on acrylic platform and the indenter was lowered at constant velocity of 30 mm/min. The experiments were conducted for each loading point five times on the same sample, and the average of the results were calculated.

Furthermore, to minimize the friction during the indentation process, the indenter and the loading surface on the specimen were covered with a thin layer of lotion. This was done due to inaccuracies and step-like data shown in the measurements.

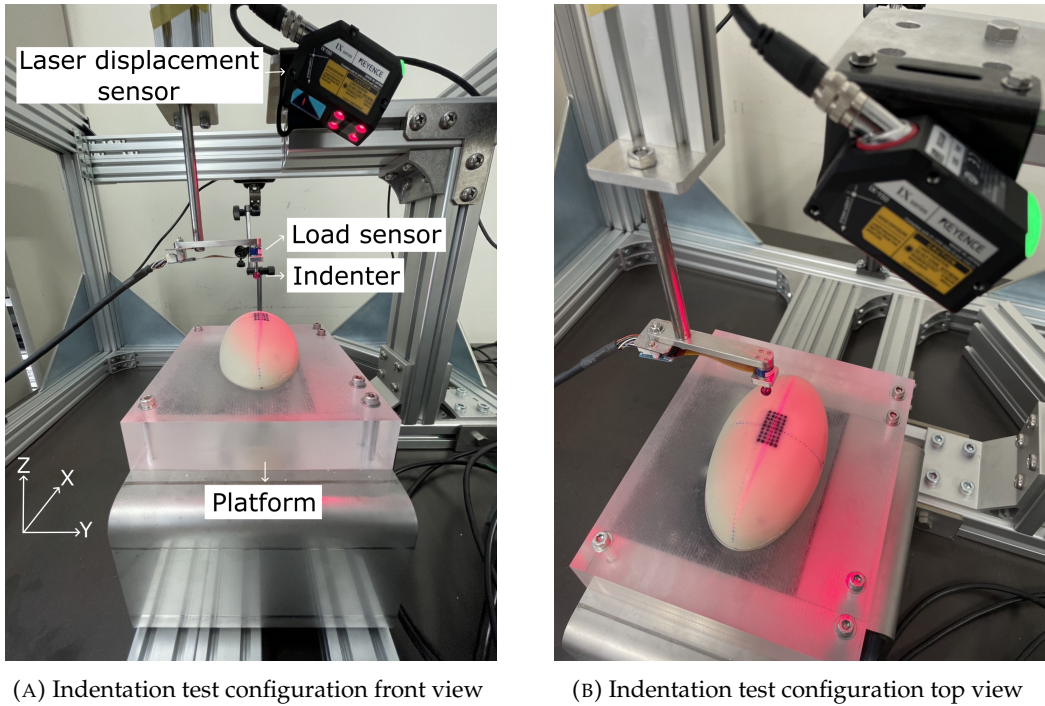


FIGURE 2.3: YNU experimental model: 6-axis sensor Test Specimen made from ultra-soft polyurethane resin positioned on a fixed platform with a similar shape for constraint.

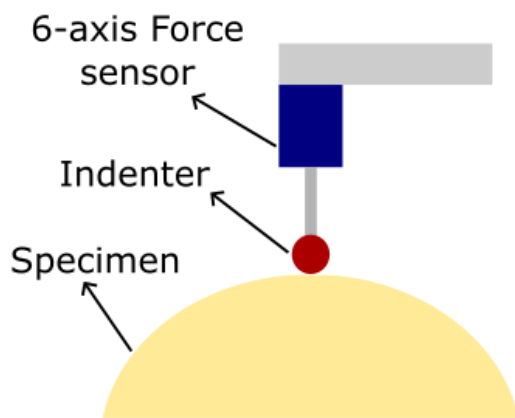


FIGURE 2.4: YNU experimental model: Loading diagram showing initial position of the indenter in normal position [21].

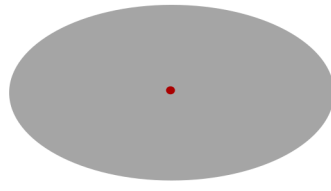


FIGURE 2.5: Middle test point: Loading point (Red point) on the top surface of the specimen.

Therefore, to reduce this measurement error, the application of lubricant was employed, ensuring a smoother and more controlled indentation process. Finally, the data was also processed and assessed using Excel.

Analysis and Comparison of Experimental Techniques

The second experimental model offers some advantages over the first model. Firstly, it enables not only the measurement of the total force reaction, but also the analysis of the force reaction components F_x , F_y and F_z . This allows for a better understanding of the material's mechanical behavior, as it allows the identification of a specific contribution of the force components and it contributes to identify other mechanisms such as viscoelasticity, plasticity, and creep. In addition, the second model allowed for the measurement of the deformation in other points near the tested loading point. This provides additional information of the material parameters, as it facilitates the characterization of the deformation behavior beyond the direct vicinity of the indentation point. Furthermore, only this test configuration makes use of a lubricant, as this experimental setup could show some inaccuracies in the first data sample.

In contrast, the first experimental model only measures the total force reaction against the indentation depth, without providing any information about the contribution of each component. While the first model allows the data gathering in simpler and more straightforward way, it may not capture the whole complexity of the material.

2.3 Experimental Tests Description

Middle Point (MP)

The first use case for the indentation test was performed at the midpoint of the major and minor axis of the ellipsoid (Fig. 2.5). This point was selected to ensure that the indentation was normal to the surface, thereby avoiding the influence of potential shear forces which could influence the measurements.

Additionally, the first indentation depth was chosen arbitrarily, for the first experimental model was $h_I = 3.8$ mm, and for the second experimental model was $h_{II} = 4$ mm. This depth was considered to be an appropriate compromise that would allow to capture the nonlinear behavior of the material, while also remaining a simple use case to reproduce in a computational model in ANSYS.

As the main objective is to find a path, which lets identify the material parameters, the most basic use case was selected and from this point the complexity was

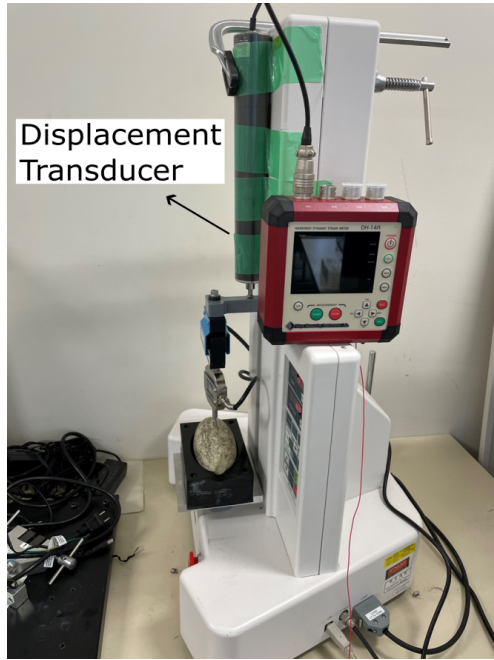


FIGURE 2.6: Load-Unload Case: Experimental model I with modified configuration setup, on top of the movable crosshead a displacement transducer was equipped to capture unloading data.

gradually built on. Through this approach, it was possible to establish a solid foundation for the subsequent experiments and data analysis.

Load-Unloading (LU)

Building on the previous test point (Fig. 2.5), an indentation test was conducted on the same point, with an indentation depth of 4 mm, but this time in a loading-unloading case.

The first experimental model setup, as described in Section 2.1, was unable to measure the displacement and force reaction during the unloading of the specimen. As a result, certain modifications were made to the experimental setup. Due to time constraints, the modification of experimental model I (EM I) was also executed by laboratory members Mori Yuta in YNU. To capture the displacement and force reaction during the unloading, a displacement transducer was equipped to the tensile and compression machine as shown in Figure 2.6.

The aim of this use case, was the observation of a possible hysteresis behavior, as well as to investigate the viscoelastic properties of the material. The load-unload test was performed at six different loading speeds, namely, 10 mm/min, 20 mm/min, 30 mm/min, 50 mm/min, 75 mm/min and 100 mm/min on the same specimen. Each speed configuration was repeated five times, and the results were averaged to reduce the effects of experimental variability.

The load-unload case helped to determine whether complex material behavior such as viscoelasticity, could be neglected for the computational model of the middle point test. The results of this experiment were used to make this decision, which has important implications for the simplification of the computational model and its accuracy and reliability.

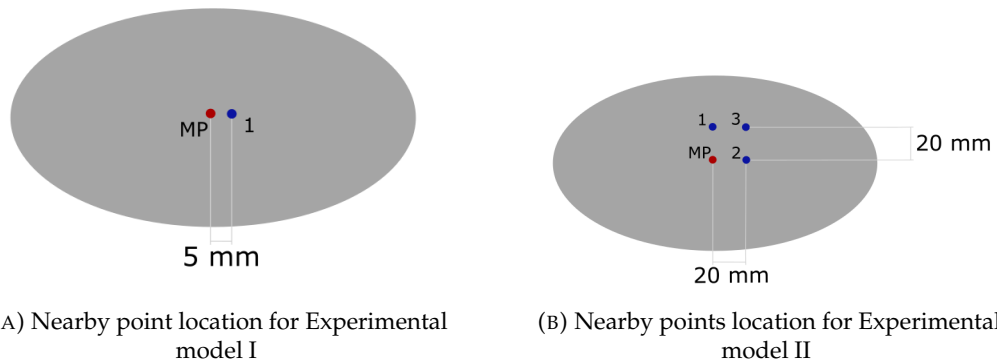


FIGURE 2.7: Nearby test point: Loading points for each experimental model to analyze shear stresses and to be employed for the validation of the computation models.

Nearby Point (NBP)

In addition to the indentation performed on the middle point of the surface, further indentations were conducted on nearby points. From these indentation tests, force-displacement curves were recorded. For each indentation the same experiment configuration, e.g., indentation depth and indentation speed, was employed as described in Sections 2.1 and 2.2.

For the first experimental model, only one nearby point located $p_{I1} = 5 \text{ mm}$ downwards of the middle point was selected as shown in Figure 2.7a.

For the second experimental model, three additional nearby points were tested. These points were located at distance of $p_{II1} = 20 \text{ mm}$ to the right, $p_{II2} = 20 \text{ mm}$ downwards, and a third point $p_{II3} = 28.3 \text{ mm}$ diagonally from the middle point forming a square (Fig. 2.7b).

The objective of these testing points was to gain a deeper understanding of the effect of the shear stresses on the indentation response. Furthermore, the results of these points allowed for the validation of the computational model and the selected material model.

2.4 Analysis and Overview of the Data and Results

In this section, the results of the experimental models described in the previous sections will be presented and analyzed. The objective is to understand the behavior of this ultra-soft polyurethane material under indentation and establish the first assumptions for the development of the computational model, as well as the material model. The section will start with a brief summary of the tests, followed by the analysis of the force-stroke curves gathered throughout the experiments.

The experimental model I served mainly as a comparator and a quick way to gain an idea of the mechanical behavior under indentation, for this model three different use cases were measured. An indentation in the middle point of the surface with an indentation depth of $h_I = 3.8 \text{ mm}$. Subsequently, the load-unload case was observed under an indentation depth of $h_{I2} = 4 \text{ mm}$, and with six different speeds ranging from 10 mm/min to 100 mm/min . Finally, a nearby point was selected near the middle point, $p_{I1} = 5 \text{ mm}$ to the right, to use it as a validation point for the selected material model.

A similar process was followed for the experimental model II (EM II), the middle point indentation was performed with an indentation depth of $h_{II} = 4 \text{ mm}$ and a indentation speed of 30 mm/min , where the force components could be observed. Similarly, the load-unload scenario was tested under the same conditions, and three nearby points were measured.

2.4.1 Middle Point

The results of the indentation test at the middle point for both experimental showed a clear nonlinear behavior. It is assumed that this material possess a elastic-plastic behavior, which in a typical load-displacement curves has four known stages [11]:

1. Nonlinear elastic (self-adjusting): In this stage, the material adjusts itself to the loading conditions, and the deformation is elastic and reversible.
2. Linear elastic: The material is bearing the external load in this stage, the deformation is still elastic and reversible
3. Nonlinear plastic (failing): With the increase of the external load, the material reaches its yield point and undergoes permanent deformation
4. Failure: The material fails leading to permanent damage.

Figure 2.8 shows the results of the two indentations at the middle point of the specimen surface. The load-displacement curves showed nearly identical material behavior for both experimental configurations. This use case demonstrate the nonlinear-elastic behavior of the material, as there was no evidence of a yield point or plastic behavior. Both curves began at zero, and the force increased gradually with increasing, resulting in a slightly concave shape.

Figure 2.8a displays all the measurements points obtained from experimental model I and its polynomial approximation. This approximation was used for the subsequent steps of the iFEM approach. The maximum total force for experimental model I at a maximum indentation depth of $u_{I,MP} = 3.8 \text{ mm}$ was $F_{I,MP} = 0.4218 \text{ N}$. For experimental model II, at an indentation depth of $u_{II,MP} = 4 \text{ mm}$, the maximum forces for each component were $F_{Z,II,MP} = 0.546 \text{ N}$, $F_{Y,II,MP} = 0.0124 \text{ N}$, and $F_{X,II,MP} = 0.0093 \text{ N}$.

From load-displacement curve of experimental model II (Fig. 2.8b) it was evident that the force reactions in the X and Y directions could be disregard, as these were considerably lower than the force reaction in Z direction. Therefore, the focus in further analysis was mainly on the force reaction in Z direction. Additionally, this case revealed that shear stresses were minimal, which is consistent with the purpose on performing the indentation with the least influence of external factors.

Figure 2.9, shows that the load-displacement curve of experimental model I has a similar initial behavior to that of experimental model II. However, as the indentation depth increases, the curve of experimental model I is positioned lower than that of the second model. One possible explanation for this difference could be the effect of aging on the material properties of the specimen used in the first model. Since the specimen used in this configuration was manufactured months before (Section 2.1), it is possible that the aging had led to a decrease in its mechanical properties, resulting in a lower resistance to deformation and therefore, lower stiffness than the newly manufactured sample. Another possible explanation could be the presence



FIGURE 2.8: Load-displacement curve experimental data for Middle Point use case for both experimental models.



FIGURE 2.9: Total Force Reaction-Displacement curve: Comparison between experimental data for Middle Point use case from both models.



FIGURE 2.10: Load-displacement curve experimental data for Load-Unload use case for both experimental models.

of external factors during the conduction of the experiments or the configuration of these. Nevertheless, as the main purpose of this Middle Point use case was to minimize the influence of these factors, this explanation seems less probable.

2.4.2 Load-Unloading

Following the Middle Point use case, in addition to the loading data, the unloading was also captured for both experiments as explained in Section 2.3. Figure 2.10 shows the load-displacement curve for experimental model I and next to it experimental model II. Both results exhibited during the unloading some degree of hysteresis, as there was a slight difference in the force reaction measured. However, the material displayed good elastic behavior, as it returned to its original shape once the indenter was removed.

The hysteresis displayed for both configurations could have occurred due to several reasons, such as viscoelastic behavior of the material, or external factors, like friction between the indenter and the specimen, surface roughness of the indenter, test configuration, and so on. To examine closer the main reason for the hysteresis, only with first experimental setup, a series of indentations tests were performed with different speeds.

Figure 2.11 shows the result of the load-unload indentation tests from the lowest to highest value for the indentation speed. It could be observed, that the curves exhibit a similar material behavior. A slight increase in the hysteresis was observed when the indentation speed was increased. Specifically, during the loading, the force reaction were slightly higher as the speed and indentation depth increased. During the unloading, the only notable difference was observed with 100 mm/min, where the unloading curve had the lowest values.

From the results and in the case of ultra-soft polyurethane, it is likely that the hysteresis is primarily due to the viscoelastic behavior of the material. Nevertheless, for the tests done in the middle of the surface, it was decided that the viscoelastic properties could be neglected for the material modeling seeing that the difference between the curves is not impactful for the first stage of the identification of the material parameters.



FIGURE 2.11: Load-Unload Use Case: Analysis of Viscoelastic material properties by using six different indentation speeds. Load-Displacement curves were obtained from the first experimental test configuration.



FIGURE 2.12: Total Force Reaction-Displacement curve: Comparison between experimental data for Middle Point and Nearby Point. This point was located 5 mm right from the midpoint, following the minor axis of the ellipsoid.

2.4.3 Nearby Point

To complement the analysis of the viscoelastic behavior of the material, a nearby point located $p_{I1} = 5$ mm to the side of the midpoint, following the minor axis of the ellipsoid (see Subsection 2.3). This location was chosen to investigate if the mechanical response of the material is uniform across the surface and if any variations could be detected within a short distance. Figure 2.12 shows the results of the Middle Point use case vs. the selected Nearby Point case for experimental model I.

The new load-displacement shows nearly identical behavior to that of the first case, except for the last part of the curve, where the Nearby Point curve goes slightly lower. The maximum force obtained for the Nearby Point case was $F_{I_{NP}} = 0.4134$ N, which is lower than the one obtained before, which was $F_{I_{MP}} = 0.4218$ N.

It can be concluded, that the results from this nearby point support the findings from the Middle point test, indicating that the material behavior was homogeneous in the region of interest. The small difference in the maximum force values could be due to the variations in the experimental conditions, e.g. the increment of the gradient of the contact surface due to the curvature of the specimen. This change could potentially affect the distribution of the stress and strains within the material. Nonetheless, these differences were not significant enough to affect the overall conclusions.

With the measurements taken in the additional nearby points for experimental model II (Subsection 2.3), it was possible to investigate whether the small variations in the results obtained with experimental model I could be attributed to the difference in the gradient of the contact surface. Figure 2.13 shows the result for each force reaction component for all four tested points. In X-direction, the maximum force was observed for point 2, which had the smallest gradient contact surface, followed by point 3. These points were 20 mm down along the X-axis, in contrast to the other two points, which were at the origin of the X-axis. For the middle point

and point 1, which had the largest contact surface gradient, the X-component force reaction was almost 0 N.

Similarly, in Y-direction, the maximum force was observed for point 3, followed closely by point 1. For the middle point and point 2 the Y-component force reaction was almost 0 N. Point 3 and point 1 were 20 mm right along the Y-axis, and the middle point and point 2 were at the origin of the Y-axis. As for the Z-direction, the maximum force was observed at the middle point, followed by point 2, and consequently with similar results point 1 and point 3. For all the points the results in Z-direction are more significant than in the other directions.

These results suggested that variation in the gradient of the contact surface may have contributed to the small differences in the results obtained with experimental model I. Specifically, it was observed, that with a smaller contact surface gradient the higher the X-component the same for the Y-component with the larger contact surface gradient. In conclusion it is possible to confirm that the material behavior was homogeneous, and that the larger the contact surface gradient became, the lower the total force reaction.



FIGURE 2.13: Nearby Point Use Case: Analysis of shear stresses by observing three different nearby points on the specimens surface. Load-Displacement curves were gathered from Experimental Model II showing each force component.

2.5 Main Assumptions for Material Modeling

In this section, the main assumptions based on the results obtained from the indentation tests will be summarized. These assumptions will be used for the development of the material models. As previously mentioned, one of the goals of this project was to develop the material model from an ideal scenario, while considering the limitations at each level. The complexity of the material model was incrementally increased until a set of material parameters that provided a proper compromise to the experimental results was obtained. Defining these levels allowed the assessment of the impact of each parameter on the development of the material model.

Based on the presented experimental data and previous discussion, the following assumptions could be made:

1. The material can be assumed to be homogeneous in the region of interest for the Middle Point Case, as the results from the nearby points support the findings from midpoint test.

2. Nonlinear elasticity is observed and hysteresis can be neglected, as the changes observed with the different loading speeds were not significant enough to affect the initial results.
3. The viscoelasticity of the material can be ignored for the first design of the material model, as the material returns to its original shape and almost no energy is lost during deformation.
4. Friction and shear stresses will be neglected, as in the Middle Point case the observed force components in x and y directions are non-relevant.

It is important to mention, that it was noted that the main assumptions made may not hold for different experiment settings, such as higher loads, longer loading times, higher temperatures, high shear stresses, and so on. Therefore, it was important to keep these assumptions in mind when using the chosen material model in a validation case.

2.5.1 Level 1: Linear Elasticity

The first level a linear elastic model was used. This model assumed that the material behaves linearly, i.e., the deformation is linearly proportional to the applied load and the material returns to its original shape after the load is removed. This model is based on Hooke's law, where the stress-strain relationship is

$$\sigma = E\varepsilon, \quad (2.1)$$

where σ is the stress, E is the elastic modulus, and ε is the strain. For the Middle Point Case, the material is assumed homogeneous and isotropic, thus the elastic modulus is the same in all directions. For an indenter with a spherical tip, the contact area A between the indenter and the specimen can be approximated as,

$$A = r_i^{\frac{1}{2}} h^{\frac{1}{2}}, \quad (2.2)$$

where r_i is the radius of the indenter, and h is the indentation depth. For a spherical indentation assuming the Hertzian contact theory, the Hertzian relationship between the applied force F and the indentation depth h is [19],

$$F = \frac{4Er_i^{\frac{1}{2}}h^{\frac{3}{2}}}{3(1-\nu^2)}, \quad (2.3)$$

where E and ν are the Young's modulus and Poisson's ratio of the indented material. This Hertzian relationship is used as the analytical basis on the contact of ellipsoid bodies in indentation experiments [19]. This model provided a simple and straightforward approach to describe the material behavior under small deformations. The elastic modulus and the Poisson's ratio are the two main parameters that will be used for this model. Additionally it was assumed that the material is near incompressible, therefore, a fixed Poisson's ratio was chosen,

$$\nu = 0.49, \quad (2.4)$$

leaving the analysis of one parameter, the elastic modulus. The linear elastic model served as a basis for the more complex material models developed in the subsequent levels, and it provided a reference point for the identification of other material parameters.

2.5.2 Level 2: Hyperelasticity

The second level introduces a higher complexity, as more material parameters are analyzed. For this level a Neo-Hookean model was used to describe the material behavior based in the strain energy potential function. The elastic strain energy potential function for the Neo-Hookean material model is given by

$$W = C_1(I_1 - 3) + \frac{1}{D_1}(J - 1)^2, \quad (2.5)$$

where C_1 is a material constant, D_1 the material incompressibility parameter, J the determinant of the elastic deformation gradient, and I_1 is the first invariant of the right Cauchy-Green deformation tensor, i.e.

$$I_1 = \lambda_1^2 + \lambda_2^2 + \lambda_3^2, \quad (2.6)$$

where λ are the principal stretches [22]. To maintain conformity with linear elasticity, the material constant

$$C_1 = \frac{\mu}{2}, \quad (2.7)$$

where μ is the shear modulus or the second Lamé parameter. If the material is assumed to be incompressible,

$$J = 1, \quad (2.8)$$

and the second term in the strain energy potential W becomes zero [23].

The Neo-Hookean model requires two main parameters to be identified; the shear modulus μ and the incompressibility parameter D_1 . The incompressibility parameter relationship with the initial bulk modulus

$$K = \frac{2}{D_1}, \quad (2.9)$$

can be defined [2]. The relationship between the shear modulus, the elastic modulus, and the Poisson's ratio

$$\mu = \frac{E}{2(1 + \nu)}, \quad (2.10)$$

can be calculated, as well as for the bulk modulus

$$K = \frac{E}{3(1 - 2\nu)}. \quad (2.11)$$

Using the results of the first level with E and ν it is possible to establish a possible range for μ and D_1 . This targeted range helped in the reduction of computational time for simulations. The hyperelastic model provides a more accurate description after the initial slope of the material behavior in comparison to linear elastic model, as this model takes into account the nonlinear behavior of the material.

3 Computational model

The previous chapter, presented the experimental model designs for the iFEM process of the material parameter identification, detailing the experimental setups, results, and main assumptions made for the material models. These foundations enabled the development of the finite element (FE) model.

In this chapter, the computational models of the indentation tests introduced in Chapter 2 will be described. These models were constructed using the finite element software ANSYS. The computational model serves as the principal link between the experimental data and the identification of the specimen's material parameters.

The initial simulation model, referred to as Computational model I (CM I), served as a tool for testing the preliminary ideas, as well as establishing the basis structure for the computational model. This first step was essential to identify the strengths and weaknesses of the model, offering insights that guided the development of an improved simulation model, referred to as Computational model II (CM II). By examining the results and challenges of computational model I, the initial conceptual ideas for FE model were iterated, leading to the creation of a more robust and accurate computational model for the material parameters' identification process.

In this chapter, the development process of the computational models will be discussed in detail, including the complications encountered, the proposed solutions, and the improvements made in computational model II.

3.1 Computational model I

3.1.1 Middle Point

The quasi-static nature of the indentation experiment for allowed the use of a static structural analysis. To prioritize the development of the framework for the material parameter identification process, the model was simplified as much as possible. This approach minimized the influence of errors arising from complex geometries and boundary conditions.

Description

The geometry only included key components that significantly contribute to the mechanical response, i.e., the indenter and the specimen. The tumor extraction geometry depicted in Figure 2.2 was also modeled for CM I. Both the indenter and the specimen utilized SOLID187 elements. SOLID187 elements are a high order 3-D, 10-node elements with three degrees of freedom at each node. These elements were suitable for simulating deformations of nearly incompressible hyperelastic materials and offered hyperelasticity, large deflection, and large strain capabilities [2].

The geometry model used for EM I is shown in Figure 3.1. Although symmetry could have been applied, it was not employed in this case. This decision considered future projects, where the measurement and identification of human organ material

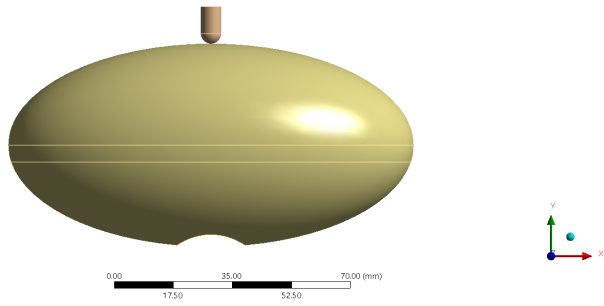


FIGURE 3.1: CM I geometry: Illustration of the geometry model with its key components, indenter and specimen with tumor extraction.

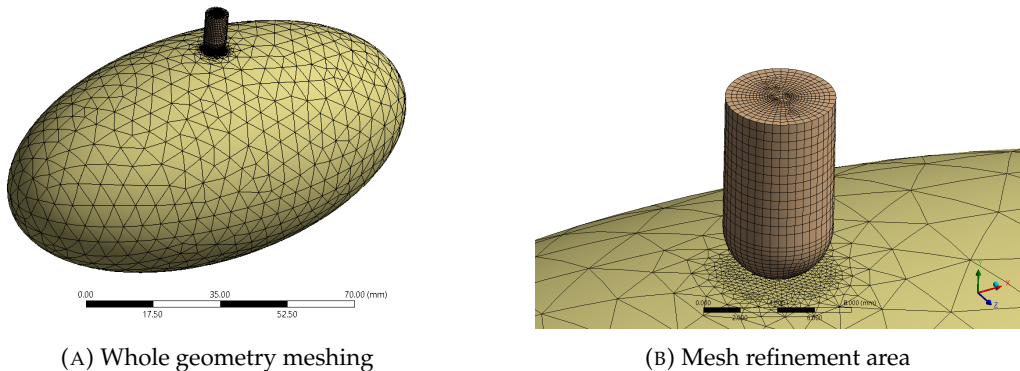


FIGURE 3.2: CM I mesh: Patch conforming mesh with contact sizing refinement in the contact between the indenter and the specimen's surface.

parameters were desired objectives. For these cases, due to the material's anisotropy and the usual complex geometry, symmetry boundary conditions could not be applied. The contact formulation between the indenter and the specimen was set to frictionless (CONTA174) to reduce overall model complexity and mimic the lubricated contact of the experiment configuration. The lower half of the specimen was defined as a fixed support, mirroring the physical constraint of the experimental setup. The displacement value h was applied to the indenter in the Y-direction, and the force reaction F was subsequently obtained.

A global element size of $e_{I_s} = 5$ mm was applied to the specimen's mesh, which consisted of quadratic tetrahedral elements. The contact area between the indenter and the specimen's surface was refined to $e_{I_a} = 0.3$ mm (Fig.3.2). The primary reason for applying contact sizing refinement was to ensure independence from the specimen's geometry or the indenter's position on the specimen's surface.

Finally, initial parameters were assigned to the computational model to approximate the mechanical properties of ultra-soft polyurethane. For the linear elasticity level, values for the Young's modulus E and the Poisson's ratio ν were assigned. From the main assumptions made in Section 2.5, the Poisson's ratio for the first level material model was set to $\nu_{LE} = 0.49$, and the Young's modulus was calculated using



FIGURE 3.3: CM I vs. EM I: Comparison of force-displacement curves between experimental data for Middle Point case and the initial computational model with a linear elastic model for $h = 2$ mm.

equation 2.3

$$E = \frac{3F(1 - \nu^2)}{4r_i^{1/2} h^{3/2}}. \quad (3.1)$$

Substituting the indenter radius $r_i = 3$ mm and the indentation depth $h = 3.8$ mm a Young's modulus E_{LE} was calculated and resulted in

$$E_{LE} = 0.018 \text{ MPa} \approx 0.02 \text{ MPa}. \quad (3.2)$$

Level 1 Results

An indentation depth of $h = 3.8$ mm could not be solved with the linear elastic material model. Through an iterative process, it was discovered that the linear elastic material model could only be applied up to an indentation depth of $h \approx 2$ mm.

The initial attempt to match the experimental and simulation data provided a reasonable approximation of the experimental data. Figure 3.3 demonstrates the comparison between the experimental data and the CM I using a linear elastic material model up to an indentation depth of $h = 2$ mm. The CM I curve displayed a more pronounced curvature than the experimental data. Additionally, at $u = 0$ mm, the experimental curve exhibited a steeper initial slope; however, as the displacement increased, the difference in slope between the two curves diminished.

This result indicated that for a displacement greater than $u = 2$ mm, the CM I curve would lie above the experimental data. Interestingly, it was observed that, despite employing a linear elastic model, the force-displacement curve exhibited a nonlinear response. This observation suggested that even a relatively simple material model could capture some degree of nonlinearity.

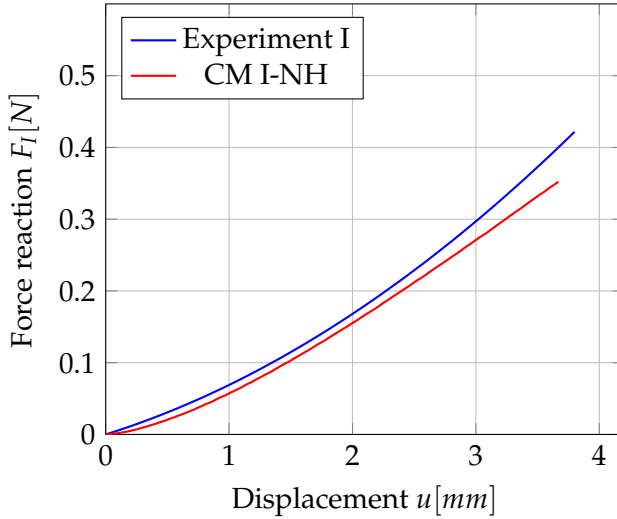


FIGURE 3.4: CM I vs. EM I: Comparison of force-displacement curves between experimental data for Middle Point case and the initial computational model with a Neo-Hookean model for $h = 3.8$ mm.

Level 2 Results

At the hyperelastic level, the initial parameters for the Neo-Hookean model, the shear modulus μ and the incompressibility parameter D_1 were calculated from the Young's modulus E_{LE} and the Poisson's ratio ν from the linear elastic model. With equations 2.10, 2.11, and 2.9, the shear modulus μ_{CMI} and the incompressibility parameter D_{1CMI}

$$\mu_{CMI} = 0.0067 \text{ MPa}, \quad (3.3)$$

$$D_{1CMI} = 6 \text{ MPa}^{-1}, \quad (3.4)$$

were calculated, respectively. These parameters were integrated in the model described above. In comparison to the linear elastic model, the Neo-Hookean material model could solve the simulation for an indentation depth of $h = 3.7$ mm. The Neo-Hookean simulation curve displayed a similar slope at lower values of u in comparison to the experimental data. As the displacement u increased, the difference in slope between the two curves increased, and from $u \approx 2.5$ mm until the end, the computational curve showed a flatter slope than the experimental curve.

Despite the discrepancies between the two curves, the Neo-Hookean provided a fair approximation to the experimental data, considered the given displacement range. Likewise, this outcome evidenced that the Neo-Hookean model was capable of capturing some of the nonlinear response observed in the experimental data, by directly inputting the calculated values from the linear elastic material model. Nevertheless, it is important to note that improvements to the computational model are necessary to achieve a more accurate representation of the experimental results.

3.1.2 Nearby Point

For the nearby point test configuration described in Subsection 2.3 was also modeled to gain an insight of the first set material parameters obtained from the middle point



FIGURE 3.5: NBP - CM I vs. EM I: Comparison of force-displacement curves between experimental data for Nearby Point case and the initial computational model with a Neo-Hookean model for $h = 3.8$ mm.

computational model. For the nearby point computational model, the Neo-Hookean model was employed, and the CM I was adapted by changing the indenter's position.

The experimental data curve from 2.4.3 and the computational model's curve are shown in Figure 3.5. Both curves exhibited a similar parabolic shape; however, the simulation curve showed once again, at a larger indentation depth, a flatter slope than the experimental data. This result presented a nearly identical behavior to that of the middle point case.

In conclusion, while there were differences, the initial calculated values provided a consistent approximation to experimental data, indicating that the computational model captures the essential features of the material's behavior. It was decided that further refinements of the material parameters may be necessary to minimize the error between the simulated and experimental curves.

3.2 Analysis and Complications

3.2.1 Verification of the Computational Model

The verification of the computational model was an important aspect of ensuring the accuracy and reliability of the simulation results. One typical approach to verify the model is to conduct a mesh convergence analysis. To reduce computational time, symmetry boundary conditions were applied, and one-quarter of CM I was used.

Mesh Convergence Analysis

The mesh convergence FE model utilized a global element size $e_{M_s} = 2$ mm for the specimen and $e_{M_i} = 0.3$ mm for the indenter. A refinement was made in the area of interest, i.e., the contact area between the indenter and the specimen's surface, with a sphere radius of $r_{M_a} = 10$ mm and an element size of $e_{M_a} = 0.5$ mm (Fig. 3.6).

The mesh convergence analysis presented challenges, as reducing the element size from 5 mm to 0.1 mm in the contact area led to unsolvable cases due to large element deformation problems, or resulted in values deviating significantly from

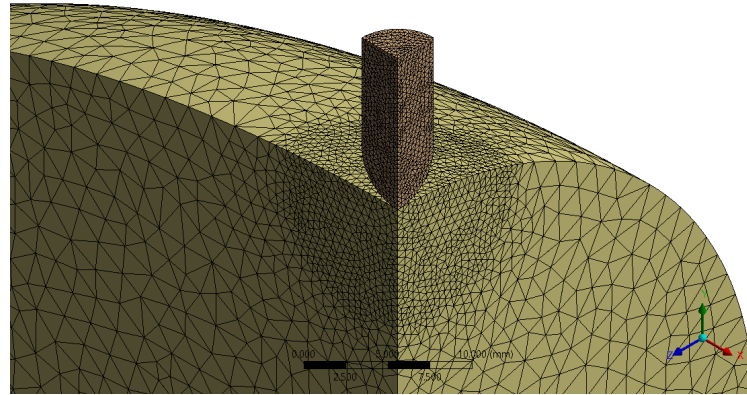


FIGURE 3.6: Mesh convergence analysis I: Mesh refinement strategy in the contact between the indenter and the specimen's surface using one-quarter of the model.

the expected convergence trend. However, a certain tendency towards convergence was observed.

Stress Distribution Analysis

The second challenge encountered during the verification process was the analysis of the stress distribution in computational model I. A classic indentation solution between an almost rigid body and an elastic body gives a Hertzian solution [19]. The expected Hertzian stress distribution was not clearly observed; instead, the stress contour plot showed rough borders, with some irregularities in the indentation surface area. This issue highlighted the need for model improvement (Fig. 3.7).

Of interest was to observe a cleaner Hertzian stress distribution in the mesh convergence FE model as shown in Figure, suggesting that the original model was not entirely reliable and the mesh dependency in the contact area.

3.3 Computational model II

The computational model II or improved computational model, addressed the challenges and observations encountered during the development of CM I. This refined model integrated the proposed solutions to the previously identified irregularities, and thus served as the final model for the iFEM approach for parameter identification.

3.3.1 Middle Point

Description

The CM II is the FE model of the experimental model II. The geometry model remained similar to CM I, featuring a spherical indenter and specimen. The tumor extraction characteristic was omitted, as the lower part of the specimen was deemed irrelevant for the overall results (Fig. 3.8a). Furthermore, in CM II, only one-half of the model was used, again taking advantage of the symmetry boundary conditions. Also, this choice was made to facilitate the visualization of the deformation profile for subsequent validation steps. Same as in CM I, the contact set as frictionless, and

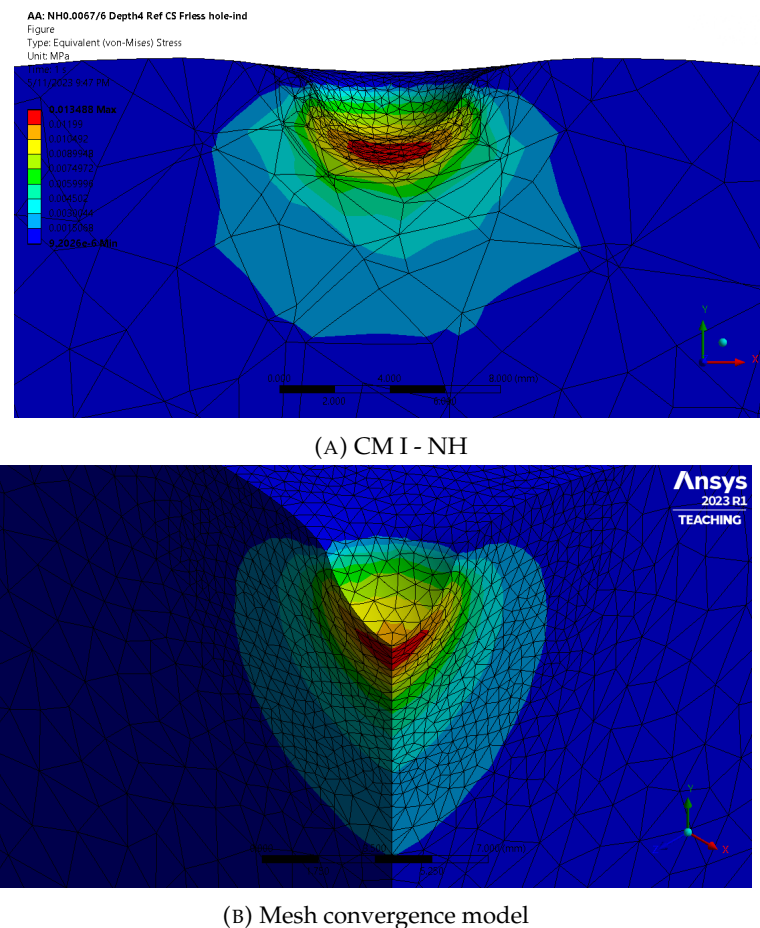


FIGURE 3.7: Stress distribution analysis of the CM I with a Neo-Hookean material model and the mesh convergence model, which shows the irregularities in the stress contour plot.

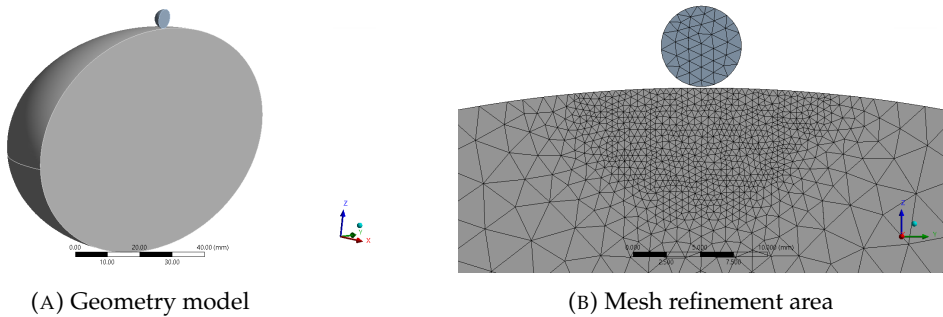


FIGURE 3.8: CM II mesh: Patch independent mesh with refinement in the contact area between the indenter and the specimen's surface.

the fixed support was applied to the lower part of the organ.

The mesh refinement for CM II was guided by the results of the mesh convergence analysis of CP I. The global element size was maintained at $e_{II_s} = 5$ mm, while the refinement area was adjusted to $e_{II_a} = 0.5$ mm with a sphere radius of $r_{II_a} = 8$ mm. The results in CM I showed that the indenter could be considered as a rigid body; therefore, the element size was set at $e_{II_i} = 1$ mm, as it did not have a significant influence on the results. To further improve the mesh quality, a patch independent method was employed, reducing the mesh's maximum skewness from 0.85 to 0.6 (Fig. 3.8b).

Large Element Deformation Strategy

To address the issue of the large element deformation for larger indentation depths, the ANSYS **nonlinear adaptive region** option was applied. This feature performed a remeshing operation in the contact area of the specimen whenever the elements reached a high distortion level. This adaptive meshing region process made it possible to conduct a successful mesh convergence analysis. In this mesh convergence analysis, all values could be calculated and convergence was reached. As a result, the element size in the contact area was determined to be changed from 0.5 mm to 1 mm.

Stress Distribution Strategy

In terms of the stress distribution, the computational model II demonstrated improvements over CM I. The new stress contour plot exhibited more clearly defined borders, and the irregularities present in CM I did not emerge on the specimen's indented surface. This resulted in a stress distribution that more closely aligned with the expected Hertzian solution. A comparative illustration of the stress distributions from CM I and CM II is displayed in Figure 3.9.

Adjustments to Deformation Behavior

During the simulated indentation process, an unusual deformation pattern was observed in the computational model. The indented mass in the model tended to move upwards, enveloping the spherical indenter, which deviated from the experimental test observations. In the real-world experiments, the indented mass seemed to displace sideways. This discrepancy was attributed to the fixed support boundary

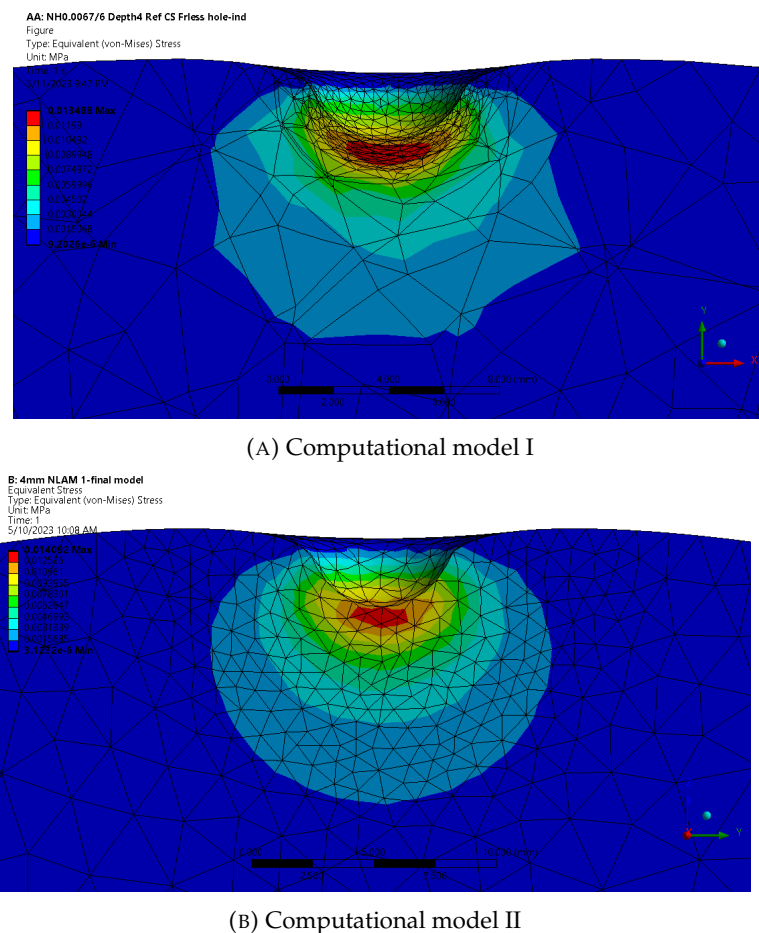


FIGURE 3.9: Comparison of stress distribution in computational models I and II with a Neo-Hookean material model after mesh strategy improvements.

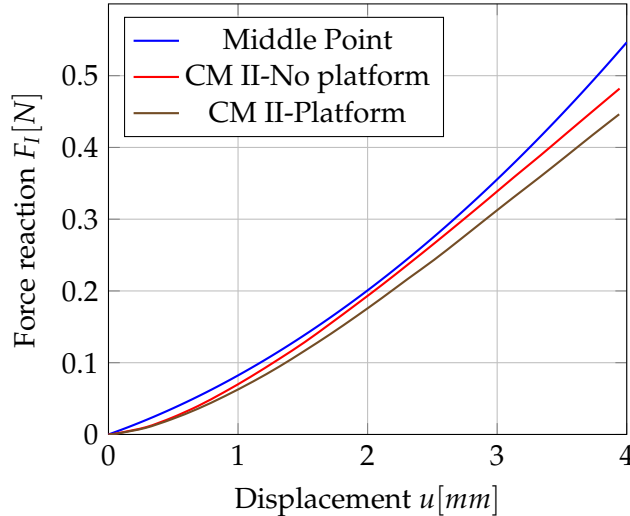


FIGURE 3.10: NBP - CM I vs. EM I: Comparison of force-displacement curves between experimental data for Nearby Point case and the initial computational model with a Neo-Hookean model for $h = 3.8 \text{ mm}$.

condition on the lower specimen's surface, which restricted lateral movement of the indented mass.

To improve this unnatural deformation pattern, a more accurate representation of the experimental setup was introduced into the FE model. The specimen was positioned on a bowl-shaped platform, mirroring the experimental configuration. The platform was designed with a slightly major radius to allow for lateral displacement of the indented mass to avoid over-constraining the specimen. The contact between the specimen and the platform was set to frictional, with a friction coefficient of 0.2, and the base of the platform possessed a fixed support.

The inclusion of the platform in the FE model had an impact on the deformation in the indentation area, as it showed a more natural deformation. Also, there was an impact on the load-displacement curve (Fig. 3.10). The curve with platform showed a better fit to the experimental data, as the overall shape of the curve was more comparable to the experimental data. Therefore, the FE model with the platform was selected as the final model for computational model II.

This chapter has presented an in-depth analysis of the development and refinement of the computational models I and II, used for simulating the indentation tests. The transition from CM I to CM II revealed the challenges encountered in an indentation simulation model and how significant is handling large element deformation for the mesh quality improvement. Specifically, the use of a nonlinear adaptive region facilitated more reliable simulation results, displaying a more closely Hertzian solution. This improvement reinforced the model's robustness for the subsequent application in an inverse finite element method approach for the identification of the material's parameters. Moreover, the adjustment in involving platform emphasized the importance of incorporating realistic boundary conditions and constraints into the computational model.

4 Inverse Finite Element Method for Material Parameter Identification

The verification of the computational model in the previous chapter was followed by the implementation of the Inverse Finite Element Method (iFEM) for material parameter identification. As outlined in Chapter 3, the Neo-Hookean material model was employed due to its ability to describe the behavior of ultra-soft polyurethane over the range of the considered deformations. Moreover, in Subsection 1.3.3 the iFEM importance for identifying material parameters for soft materials was explained.

In this chapter, the process of parameter identification using this technique will be detailed. Firstly, the initial parameter estimation process will be discussed, followed by the optimization process. This revolved around iteratively refining the material parameters to achieve the best match to the experimental load-displacement data of EM II. The two methods explored were ANSYS Response Surface Optimization (RSO) and a custom MATLAB routine. Lastly, the implementation and development of these optimization strategies, and their strengths and weaknesses, will be discussed.

4.1 Response Surface Optimization

The Response Surface Optimization is a technique used in ANSYS for optimizing a design by creating a response surface, which represents the relationship between the design variables and the objective function or performance criteria. The objective of this feature is to find the optimal set of design variables that maximize or minimize the objective function.

The process to find parameters using the RSO in ANSYS generally involves the following steps:

1. Define the design variables: The variables that influence the design are identified, e.g., geometric parameters, material properties.
2. Define objective function: The parameter or objective which will be maximized or minimized is defined, e.g., stress, force reaction, volume.
3. Define constraints: Constraints or limitations are specified, such as lower or upper bounds.
4. Generate Design of Experiments (DOE): Set of sample points are generated by varying the design variables. The DOE aims to set a design a space efficiently to capture the relationships between the input and output parameters. Simulations are then performed for each set of design variables in the DOE.

5. Create a Response Surface: Based on the results of the simulations, the software constructs a surface by interpolating the discrete sampling points from DOE.
6. Optimize the design: The optimal set of design variables are searched with optimization algorithms by iteratively evaluating the response surface and adjusting the design variables. The default optimization algorithm in ANSYS is the Multi-Objective Genetic Algorithm (MOGA), which supports multiple objectives and constraints. This algorithm aims to find a global optimum for the given problem [12].
7. Verify the candidate points: The given candidate points from the optimization tool are verified to observe if these satisfy the constraints and meet the target criteria.

For this research, the design, or input variables were the material properties from the Neo-Hookean material model, the shear modulus μ and the incompressibility parameter D_1 . The output parameters were the maximum force reaction in Z-direction F_z and the maximum directional deformation in Z-direction u_z .

Based on the observation made in Chapter 2 regarding the impact of the force components in EM II, only the values for the Z-direction were considered. Consequently, the other force components could be neglected for this particular case. The prioritization of the Z-direction values came from their maximal influence on the outcomes.

Initial Parameter Range

The initial parameter ranges for the input variables of the RSO were established based on literature review. Ultra-soft polyurethane, depending on its composition, can have a wide range of mechanical properties [30]. From the literature review a Young's modulus range for this material was 10 000 Pa to 100 000 Pa, and the Poisson's ratio range was 0.36 to 0.49. As derivated in the previous chapter in Subsection 3.1.1 with the equations 2.10, 2.11, and 2.9, the shear modulus μ and the incompressibility parameter D_1 ranges were calculated. The corresponding full ranges (FR) were 3356 Pa to 36 765 Pa and 1 MPa^{-1} to 168 MPa^{-1} , respectively.

Sensitivity Analysis

The RSO generated a response surface that enabled the performance of a sensitivity analysis. The sensitivity analysis helped identify which design variables had the most impact on the objective function or performance metric, i.e., it was possible to observe how much an objective changed when each input variable changed. By evaluating the sensitivity of the function to variations in the design variables, it was possible to prioritize the most influential parameters and understand their influence in the model during the optimization process.

By examining a local sensitivity bar diagram and a response surface, the sensitivity analysis was conducted. Figure 4.1 displays the local sensitivity bar diagram for the design variables μ and D_1 , in relation to the output parameters, namely the maximum force reaction in Z-direction F_z and the maximum directional deformation in Z-direction u_z .

The local sensitivity bar diagram provided a quantitative measure of the relative impact of the material parameters. This diagram indicated that the shear modulus

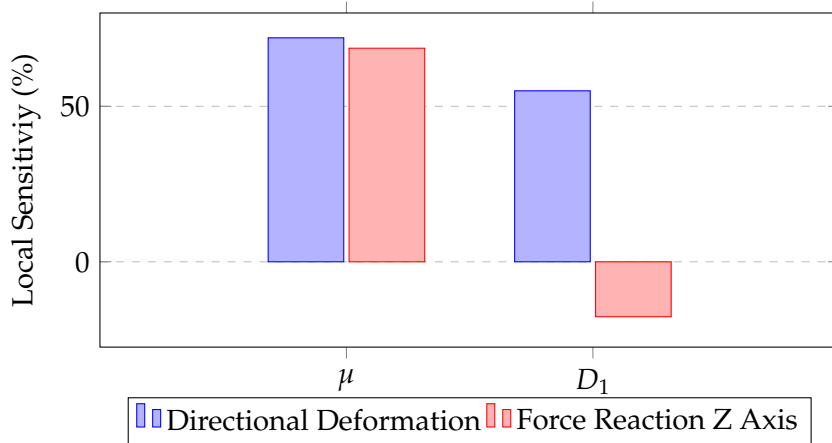


FIGURE 4.1: Local sensitivity analysis displaying the influence of the shear modulus and incompressibility parameter for the directional deformation and force reaction in Z-direction.

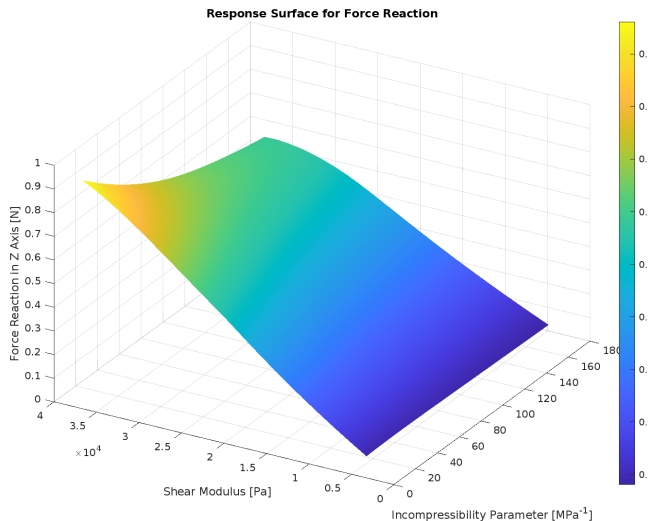


FIGURE 4.2: Response Surface for the Neo-Hookean parameters μ and D_1 in relation to the force reaction in the Z-axis.

has a positive correlation with both the force reaction and the directional deformation. I also highlighted the considerably greater impact of the shear modulus on the force reaction, nearly four times as much as the incompressibility parameter. Moreover, D_1 exhibited an inverse negative correlation with force reaction. In terms of deformation, both μ and D_1 showed a positive correlation. However, the impact of the shear modulus slightly surpassed that of the incompressibility parameter.

The response surface (Fig. 4.2) reinforced the findings obtained from the local sensitivity diagram. The steeper gradient of the shear modulus signified its greater impact on the force reaction. The incompressibility parameter, on the other hand, exhibited a steeper slope at the beginning, but it tended to flatten and almost converged. This indicated a lowering influence on the force reaction.

Initial RSO Results and Analysis

The primary performance metric or objective for the RSO was to match the maximum force in the Z-direction, observed experimentally at a displacement of $u_z = 4\text{ mm}$. The initial RSO process offered three candidate sets of material parameters, with shear modulus values around 0.011 MPa and incompressibility parameter values of 50 MPa^{-1} , 112 MPa^{-1} , and 161 MPa^{-1} . Nevertheless, these candidates did not match with the experimental maximum force when verified. Moreover, it was observed that ANSYS tended to offer only higher values for D_1 and ignored the lower half of the range. This led to a decision to refine the parameter ranges further.

The refined or reduced ranges (RR) were from 7500 Pa to 9500 Pa for the shear modulus and 1 MPa^{-1} to 10 MPa^{-1} for the incompressibility parameter. The new candidates from the RSO had a μ around 0.085 MPa and D_1 of 2 MPa^{-1} , 5 MPa^{-1} , and 7 MPa^{-1} .

Furthermore, it was observed that the maximum total deformation of the specimen did not fully reach the displacement of 4 mm , therefore a new target was modified and set for a displacement of $u_z \approx 3.9\text{ mm}$.

Assessment and Process Optimization

For each simulation curve obtained, the Root Mean Square Error (RMSE) was calculated. The RMSE is considered a commonly used metric to evaluate the differences between the predicted and observed values in the experiments. This function measured the standard deviation of the residuals or prediction errors. The RMSE is given by the formula

$$\text{RMSE} = \sqrt{\frac{1}{n} \sum_{i=1}^n (y_i - \hat{y}_i)^2}, \quad (4.1)$$

where y_i is the observed or experimental value, \hat{y}_i is the predicted or simulated value, and n is the number of data points. However, since the RMSE is scale-dependent, it was normalized by dividing the RMSE value with the mean of the observed values

$$\text{NRMSE} = \frac{\text{RMSE}}{\bar{y}}. \quad (4.2)$$

Although the RSO proved to be useful, the obtained candidates were not providing a satisfactory match to the entire load-displacement curve when using only a single point as the optimization target. This motivated the introduction of more targets along the curve in addition to the force reaction at $u_z = 3.9\text{ mm}$, specifically at $u_z = 2\text{ mm}$, and later an additional target at 3 mm was also tested.

Initially, the force reactions at 2 mm and 4 mm indentation depths were used as targets. The range of the shear modulus for this two-point (2P) target was set to 6000 Pa to $10\,000\text{ Pa}$, while the range of the incompressibility parameter was set to 1 MPa^{-1} to 6 MPa^{-1} .

Subsequently, a third target was introduced at 3 mm indentation depth, and the ranges for μ and D_1 were revised to 9000 Pa to $15\,000\text{ Pa}$ and 1 MPa^{-1} to 50 MPa^{-1} , respectively.

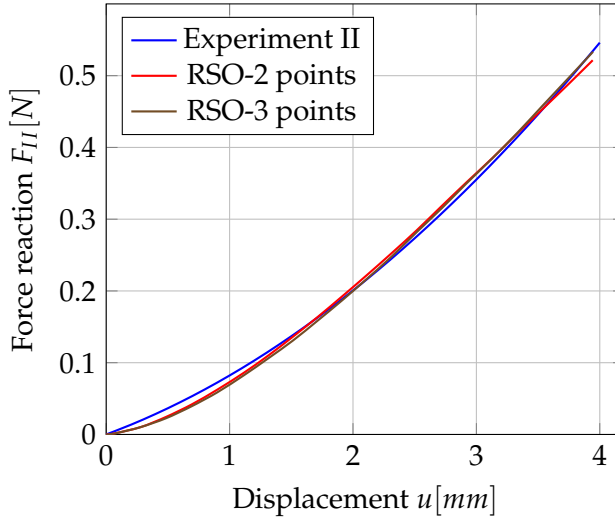


FIGURE 4.3: Analysis of multi-objective target optimization, 2 and 3 sought targets were introduced in the RSO process.

The RSO for the two-point target optimization gave a $\mu_{2p} = 9999.7 \text{ Pa}$ and a $D_{1_{2p}} = 5.8 \text{ MPa}^{-1}$. In comparison, the three-point (3P) target optimization yielded a $\mu_{3p} = 10867 \text{ Pa}$ and $D_{1_{3p}} = 47.2 \text{ MPa}^{-1}$.

Despite the differences in the estimated material parameters, the simulation curves obtained from these parameter sets were nearly identical, as shown in Figure 4.3. Furthermore, the RSO exhibited the tendency to select higher values from the range of the incompressibility parameter.

Given that the two-point and three-point target optimizations had comparable results, the optimization was continued with the two-point target optimization. This decision was driven when considering the computational cost, as this requires fewer simulations than the three-point target optimization.

4.2 Minimizing the Objective Function

In addition to the RSO, a separate identification process was conducted with MATLAB to find the global minimum of the objective function. The objective function was defined as the NRMSE, which quantifies the difference between the simulated and experimental responses.

The MATLAB optimization used the data from the RSO calculated error measurements to approximate the objective function as a surface in a three-dimensional space in relation to the design variables.

Using data from approximately 35 simulations, a surface was generated where the X-axis represented the shear modulus, the Y-axis represented the incompressibility parameter, and the Z-axis represented the NRMSE of each simulation. The Mean Relative Error (MRE)

$$\text{MRE} = \frac{1}{n} \sum_{i=1}^n \left| \frac{y_i - \hat{y}_i}{y_i} \right|, \quad (4.3)$$

was also calculated for each simulation, and the same surface approximation method was applied. The approximation was performed with a second and fourth degree polynomial. Figure 4.4b shows the surface plot of a fourth-degree polynomial with

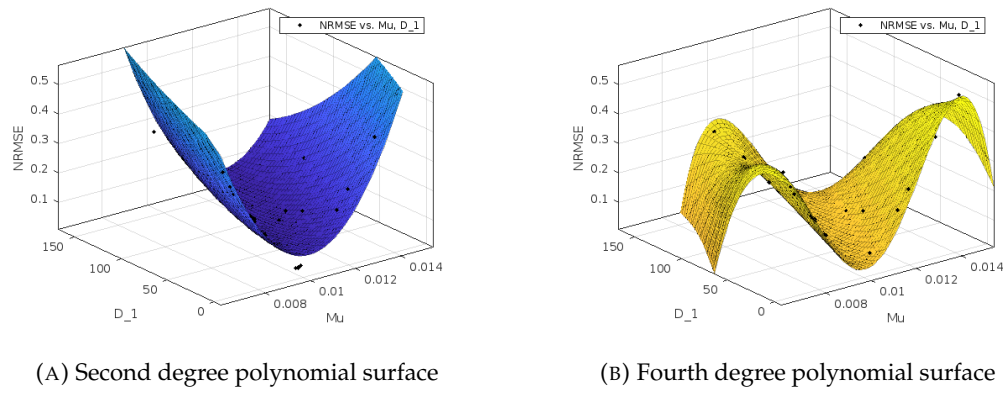


FIGURE 4.4. Surface approximation method with a second and fourth degree polynomial for NRMSE.

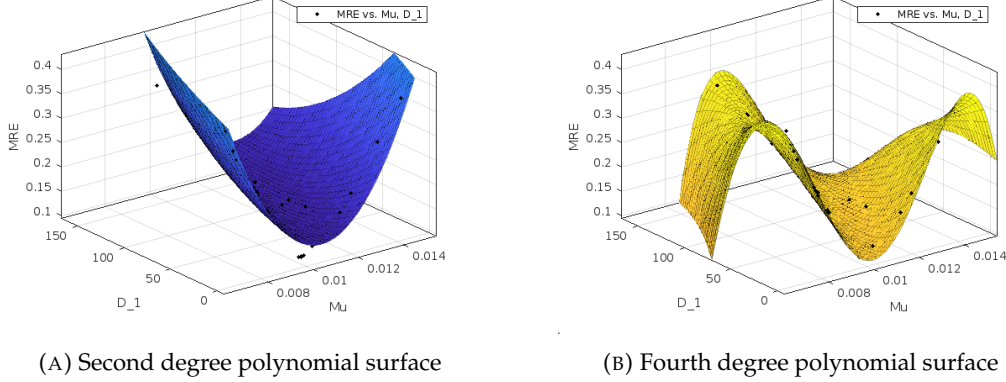


FIGURE 4.5: Surface approximation method with a second and fourth degree polynomial for MRE.

15 variables for the NRMSE. The fourth degree polynomial function had the following form

$$f(x) = p00 + p10x_1 + p01x_2 + p20x_1^2 + p11x_1x_2 + p02x_2^2 + \\ p30x_1^3 + p21x_1^2x_2 + p12x_1x_2^2 + p03x_2^3 + \\ p40x_1^4 + p31x_1^3x_2 + p22x_1^2x_2^2 + p13x_1x_2^3 + p04x_2^4. \quad (4.4)$$

The results obtained from the different polynomial degrees and the two performance metrics were summarized in Table 4.1.

Polynomial Degree	Error Metric	μ (Pa)	D_1 (MPa $^{-1}$)
2	NRMSE	12200	108.6
4	NRMSE	10600	29.6
2	MRE	11900	72.7
4	MRE	10200	1.1

TABLE 4.1: Shear modulus and incompressibility parameter obtained from different polynomial degrees and error metrics using MATLAB script.

This revealed that varying the polynomial degree and the performance metric can influence the estimated material parameters. A higher polynomial degree

tended to result in a lower shear modulus and incompressibility parameter. Furthermore, using the MRE as the performance metric resulted in lower estimates for these parameters.

4.3 Comparison between RSO and MATLAB Optimization

During the parameter identification exploration process, both RSO and MATLAB-based optimization proved to be valuable tools with their own distinct strengths and weaknesses. The combined use of these methods complemented the overall analysis of their application in the iFEM process.

The RSO in ANSYS provided a relatively user-friendly interface which did not require a background in programming, while its integration in ANSYS generated an intuitive workflow. Moreover, the RSO included built-in tools for the sensitivity analysis, which provided valuable information and insights into the relationship between the design variables and the output parameters. However, the RSO offered less flexibility compared to a custom-coded MATLAB optimization routine, and there was the need to reduce the number of the design variables and their constraints to achieve an adequate result.

MATLAB strengths relied on its highly customizable approach for problem-solving. In addition, the advanced tools for data analysis and visualization were useful to generate some direct relationship with the performance metrics. Still, MATLAB demanded software expertise, and importing the data from ANSYS introduced some time cost. Furthermore, for an accurate polynomial approximation, an increase in data points and preparation was necessary.

In conclusion, the choice between RSO and MATLAB optimization depends on the specific requirements of the study, the complexity of the problem, and the resources and skills available. This study complemented both methods to provide a more comprehensive parameter estimation. Consequently, the best material parameters identified through the RSO and the MATLAB-based optimization were inserted into the computational model for evaluation. The performance of these parameter sets was compared against the experimental data to determine their suitability.

5 Results

This chapter presents the findings from the methodologies employed throughout this study. The focus of the research was to identify the material parameters of ultra-soft polyurethane effectively. The results obtained offered critical insights into the approach's efficacy and potential limitations.

In the first section, the performance metrics applied were examined. These metrics provided a quantifiable measure of the validity and reliability of the material parameter sets identified, offering a robust means of assessing the approach's accuracy.

Subsequently, a thorough analysis of the three validation cases are detailed. These cases contributed significantly to select the best material parameter set and assess the applicability of the material parameters in other use cases.

This is followed by a detailed exposition of the framework proposed in this study for the material parameter identification process based on an iFEM approach.

Lastly, the limitations and implications of the results are listed. By identifying the constraints of the results, a well-rounded perspective of the findings was presented to further refine the process for future research.

5.1 Overview and Analysis

Upon applying the RSO and MATLAB optimization to identify the optimal material parameter set, multiple sets were calculated. Each simulation deployed various Neo-Hookean parameters sets and had a unique load-displacement solutions. These load-displacement curves were juxtaposed with the experimental data and the RMSE and NRMSE (Equation 4.1 and 4.2) was calculated to quantify the quality of each solution. To deepen the evaluation, additional performance metrics were incorporated: Mean Relative Error (MRE) (Equation 4.3), Mean Absolute Percentage Error (MAPE)

$$\text{MAPE} = \frac{100\%}{n} \sum_{i=1}^n \left| \frac{y_i - \hat{y}_i}{y_i} \right|, \quad (5.1)$$

and Relative Root Mean Square Error (RRMSE)

$$\text{RRMSE} = \sqrt{\frac{1}{n} \sum_{i=1}^n \left(\frac{y_i - \hat{y}_i}{y_i} \right)^2}. \quad (5.2)$$

Performance metrics are critical for evaluating the predictive accuracy of the computational model. These metrics provide insights into how well the model's prediction align with the experimental data. The combination of these metrics allowed for a more comprehensive assessment of all the simulations performance. For instance, the RMSE and NRMSE measured the absolute deviation of the predicted values from

the observed data, providing an overall measure of the computational model accuracy. On the other hand, metrics like MRE, MAPE, and RRMSE are useful when considering relative errors. These metrics weighed errors in relation to the actual size of the actual values [24].

The simulation results that produced the lowest performance metrics were set aside as possible optimal candidates. In particular, the parameters with the lowest NRMSE, MRE and RMSRE were investigated. Moreover, a set with an elevated incompressibility parameter was chosen for analyzing its influence on validation cases. The parameters that were determined to provide the best fit to the experimental data based on these assessments were listed on Table 5.1.

Set	μ (Pa)	D_1 (MPa $^{-1}$)	NRMSE	MRE	RRMSE	Optimization Method
1	9999.7	5.8	0.0339	0.1098	0.2067	RSO 2P RR
2	9975.2	5.3	0.0340	0.1097	0.2069	RSO 2P RR
3	10200	1.1	0.0533	0.1139	0.1964	MATLAB Poly 4 MRE
4	12453	139.3	0.0648	0.1713	0.2592	RSO 2P FR

TABLE 5.1: Neo-Hookean material parameter sets that demonstrated the best fit to the experimental data of the EM II.

Assessment of Performance Metrics

Defining good performance metrics values required a multi-dimensional approach. Firstly, the load-displacement curves' visual inspection revealed a close approximation to the experimental data (Fig. 5.1).

The load-displacements curves illustrated that the initial slope of EM II was steeper compared to all calculated candidate sets. As the displacement increased sets 1 through 3 intersected the experimental curve. Set 1 and 2 were nearly identical, initially exhibited an increasing slope, yet displayed a tendency to flatten towards the end of the curve, intersecting the experimental curve a second time.

On the other hand, set 3 crossed the experimental curve around $u = 1.5$ mm, showcasing a steeper slope relative to the experimental curve.

Set 4 displayed a pronounced curvature at the outset, followed by an increase in steepness of its slope. However, it remained constantly below throughout the experimental data.

In addition to the visual analysis, the mean of the performance metrics for all models were calculated and compared to its lowest value. Similarly, a baseline model of each performance metric was calculated and also compared to the candidate sets (Table 5.2).

To clarify, the lowest value of the NRMSE was 0.0339. The mean NRMSE across all models was 0.1662, suggesting that models with an NRMSE below this value outperformed the average. Consequently, the baseline NRMSE, represented a simple model predicting the mean load-displacement, was 0.6835, indicating that models with an NRMSE below this value surpassed the baseline model.

Given the proximity of the values among all candidates, except for set 4, it was initially inferred that utilizing NRMSE as the sole performance metric would be adequate for evaluating the goodness of fit in this specific case, an indentation of $h = 4$ mm at the center of the surface.

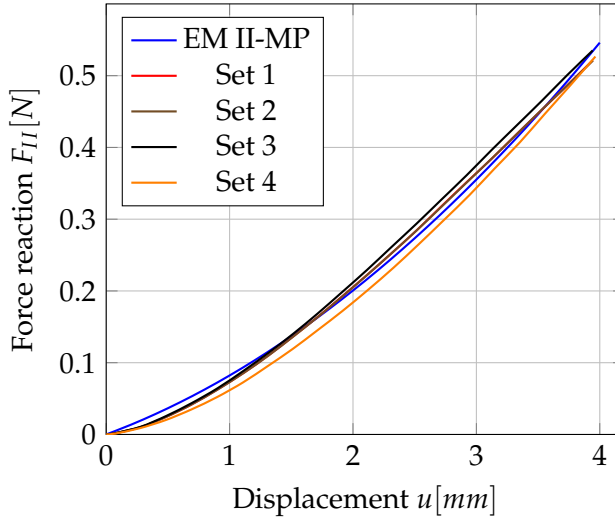


FIGURE 5.1: Visual analysis of the load-displacement curves of the best material parameter sets with the lowest NRMSE, MRE, and RRMSE and the experimental data.

Metric	Set values	Mean	Baseline
NRMSE	0.0339	0.1662	0.6835
	0.0340		
	0.0533		
	0.0648		
MRE	0.1098	0.2689	0.5916
	0.1097		
	0.1139		
	0.1713		
RRMSE	0.2067	0.2688	0.6835
	0.2069		
	0.1964		
	0.2592		

TABLE 5.2: Comparison of the performance metric of each candidate set with their mean value and baseline model value, extracted from all calculated simulations.

5.2 Validation of Computational Model

In order to confirm the reliability and effectiveness of the identified material parameters, two distinct validation cases were performed. The first validation case (VC I) involved the alteration of the indentation depth, changing it to 8 mm from the original 4 mm. This case aimed to assess how well the material model could adapt and represent the mechanical behavior with increased deformation.

The second validation case (VC II) revolved around the deformation profile of the specimen. The aim here was understand the accuracy in predicting the actual deformation shape of the specimen under indentation. This provided deeper insights into the effects of the selected incompressibility parameters.

The experimental models for the validation cases followed the same procedural

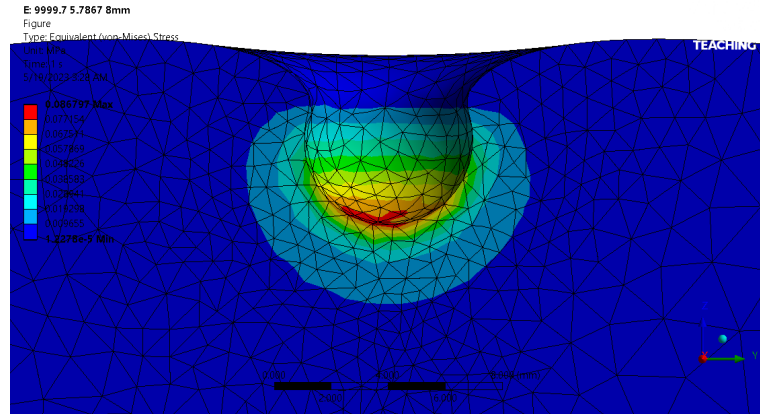


FIGURE 5.2: Stress distribution and meshing for the first validation case with an indentation depth of $h_{VC1} = 8 \text{ mm}$.

guidelines described in Chapter 2 for experimental model II. Furthermore, for the validation cases only Sets 1, 3 and 4 were evaluated (Table 5.1). As set 2 demonstrated nearly identical results as set 1, it was not considered for the validation process.

5.2.1 Deeper Indentation

The first validation experiment featured an indentation depth of $h_{VC1} = 8 \text{ mm}$, doubling the previous indentation depth of $h = 4 \text{ mm}$ at the center of the specimen's surface or middle point. Computational model II, described in Chapter 3, was used with the adjusted indentation depth (Fig. 5.2).

To facilitate the comparison of the remaining candidates, the load-displacement curves for the set 1 with the lowest NRMSE, set 3 with the lowest RRMSE, and set 4 with the highest incompressibility parameter, were plotted against the experimental data, as shown in Figure 5.3.

The load-displacement graph showed that the experimental data displayed again a steeper initial slope than the computational models. Sets 1 and 3 curves intersected the experimental curve around a displacement of $u = 2 \text{ mm}$, whereas set 4 intersected at about $u = 3 \text{ mm}$.

As displacement increased to $u = 4 \text{ mm}$, the curves for sets 1 and 3 began to flatten and fell beneath the experimental curve, while set 4 maintained its steepness and remained above. At a displacement of $u = 8 \text{ mm}$, set 4 with a maximum force of $F_{4,max} = 1.3951 \text{ N}$ managed to produce the closest approximation to the maximum experimental force $F_{II,max} = 1.283 \text{ N}$.

The new NRMSE values were significantly higher than those of the first case (Table 5.3). Noteworthy, set 3, with a lower NRMSE for the first case, and set 4 with a higher D_1 exhibited a better NRMSE performance for this case, in contrast to set 1, which had shown the best performance for the $h = 4 \text{ mm}$ indentation.

This suggested that the identified parameters may not be able to capture the behavior of the material at larger indentations. Therefore, a case-specific parameter identification for accurate modelling of larger indentations would be required.

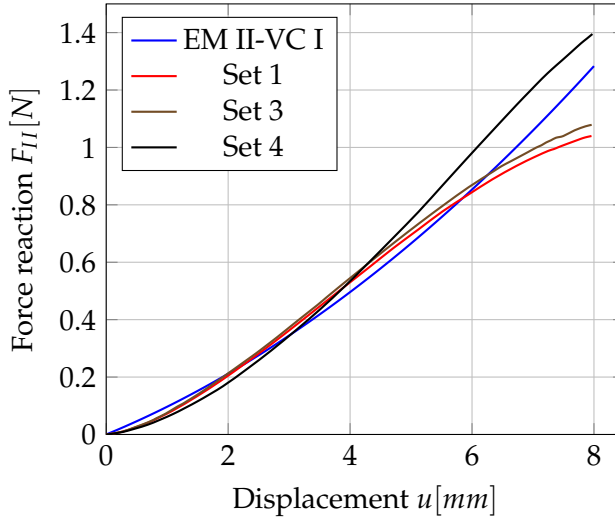


FIGURE 5.3: Analysis of the load-displacement curves of the best material parameter sets and the experimental data for the first validation case with a deeper indentation.

Set	μ (Pa)	D_1 (MPa $^{-1}$)	EM II NRMSE	VC I NRMSE
1	9999.7	5.8	0.0339	0.1503
3	10200	1.1	0.0533	0.1116
4	12453	139.3	0.0648	0.1425

TABLE 5.3: Comparison of the NRMSE calculated for the EM II and for the first validation case with a deeper indentation.

5.2.2 Deformation Profile Analysis

The second validation case evaluated the deformation profile of the specimen for the first indentation case of $h = 4$ mm in the middle of the specimen's surface. The goal was to understand how the selection of the incompressibility parameter, linked to the bulk modulus, influenced the deformation shape under indentation.

To capture the deformation shape of the specimen, the displacement of the points along an axis positioned 5 mm parallel to the X-axis were calculated (Fig. 5.4). This reference line was chosen to avoid any optical interference caused by the indenter during the laser measurements, as illustrated in Figure 5.5b. Figure 5.5 illustrates the experiment conducted by YNU. Using the marked points as reference, the laser displacement meter captured the specimen's shape along the parallel axis both before and during the indentation process. This allowed for the measurement of the deformation profile at intervals of 1 mm throughout the indentation until reaching the maximum depth of 4 mm was reached (Appendix A).

From the results calculated with the computational model II for the middle point case, a method to capture the deformation profile for the second validation case was required. However, tracking specific points on the surface of the simulation was challenging due to the remeshing process of the nonlinear adaptive meshing option utilized in the model. This process did not support the measurement of the displacement for a specific node, as the position of the node changed throughout the execution of the model's calculation.

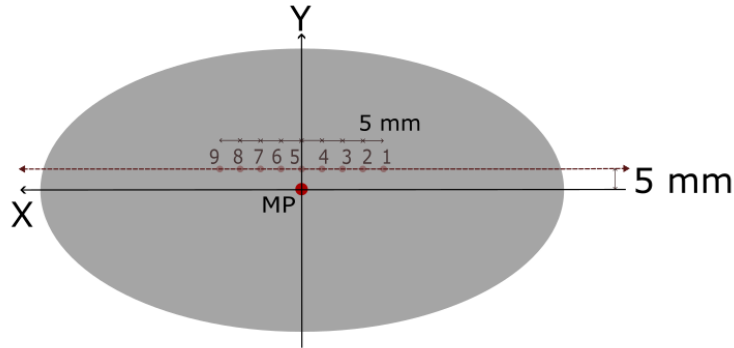


FIGURE 5.4: Deformation profile measurement diagram for the second validation case, showing the measured points along the parallel to X-axis.

To overcome this issue, a section plane was created, located 5 mm to the right of the symmetry axis, similar to the experimental model. Probe points were then selected around the deformed surface within this plane (Fig. 5.6).

The deformation profiles for the remaining candidate sets were compared with the experimental data, as shown in Figure 5.7. Although all computational models showed some degree of misalignment with the experimental data, the position of maximum deformation, Point 5 next to middle point, had a close match for sets 1 and 3.

Further, as the incompressibility parameter decreased, the overall deformation decreased. The NRMSE values for this case were listed on Table 5.4. The NRMSE results revealed that the set 3 had the best value followed closely by set 1. This validation case showcased that the selection of the range set for the iFEM process impacts the deformation response, even though the influence of the incompressibility parameter on the force reaction results was relatively minor.

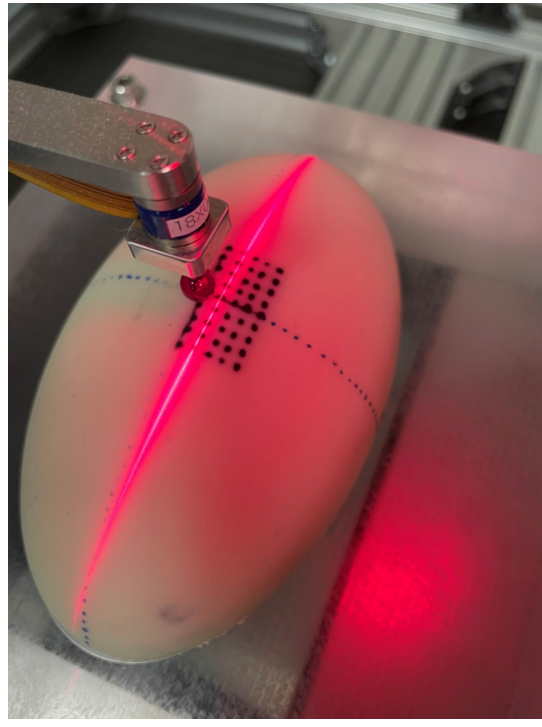
Set	μ (Pa)	D_1 (MPa $^{-1}$)	EM II NRMSE	VC II NRMSE
1	9999.7	5.8	0.0339	0.3126
3	10200	1.1	0.0533	0.2810
4	12453	139.3	0.0648	0.5645

TABLE 5.4: Comparison of the NRMSE calculated for the EM II and for the second validation case for the deformation profile curves.

Based on the combined results of both validation cases and their NRMSE values, set 3 with a shear modulus $\mu = 10\,200$ Pa and the incompressibility parameter $D_1 = 1.1\text{ MPa}^{-1}$ was identified as the best overall choice. This material parameter set captured with good agreement the indentation for EM II, and showed the best results for the deformation profile validation case and the deeper indentation case.

5.2.3 Nearby Point - Blue Point

After identifying set 3 as the best candidate from the initial two validation cases, this parameter set was subjected to a third validation test. This experiment was conducted on a nearby point, referred to as the blue point (BP), situated at a diagonal



(A) Experimental setup with laser displacement meter measurement



(B) Interference from the indenter of the measurements along the main X-axis

FIGURE 5.5: Deformation profile experiment setup performed by YNU to capture the shape of the specimen during the indentation test.

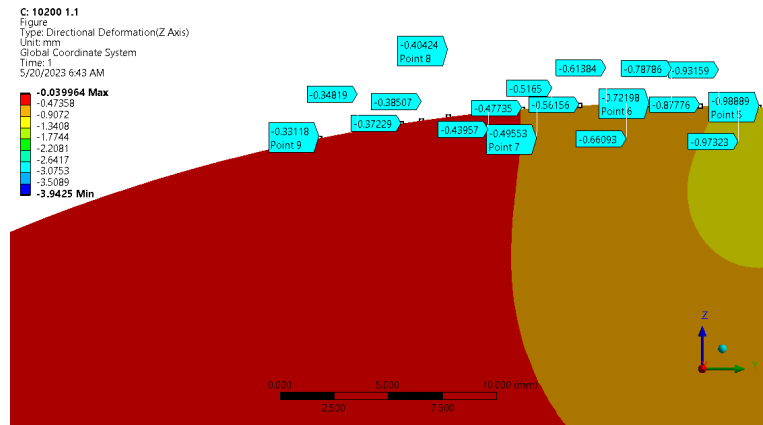


FIGURE 5.6: Deformation profile measurement in the computational model with aid of probes along the surface of the section plane located 5 mm next to the X-axis.

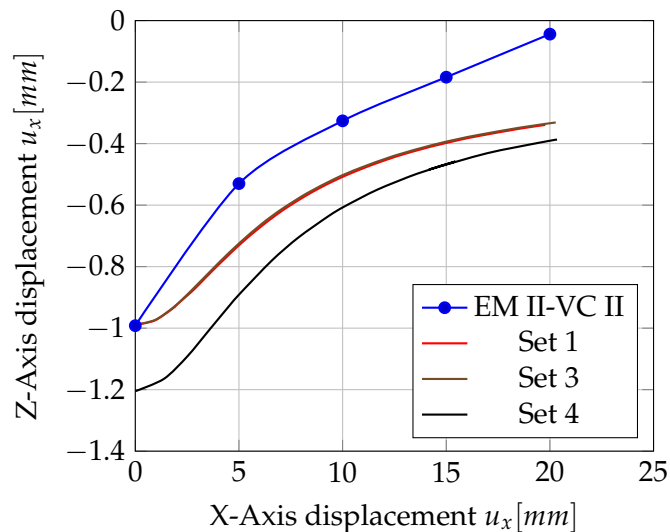


FIGURE 5.7: Analysis of the deformation profile curves of the best material parameter sets and the experimental data for the second validation case.

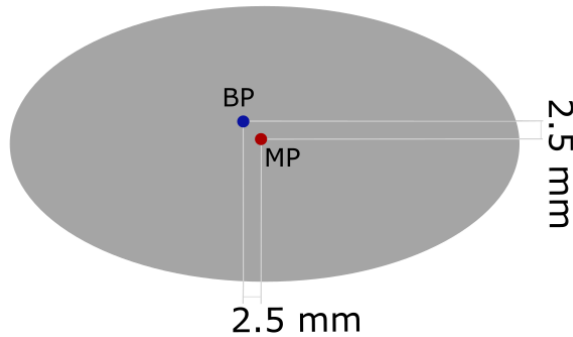


FIGURE 5.8: Blue point position diagram for the third validation case to evaluate the prediction of all force components.

distance of approximately 3.5 mm from the middle point, as illustrated in Figure 5.8.

To mimic the conditions of the experimental model II, the indentation depth was kept at $h_{VCIII} = 4$ mm. Based on the insights acquired from the deeper indentation validation case, it was considered prudent to maintain this depth to ensure that the selected material parameters would accurately represent the behavior of the specimen for this new indentation point.

In this use case, unlike the previous ones, the full computational model was required, as shown in Figure 5.9. The symmetry boundary conditions used before were not applicable due to shifted indentation position. With exception from these conditions the blue point model followed the process as computational model II, described in Section 3.3.

Furthermore, it was anticipated based on previous nearby point experiments that force components in x and y directions would become significant the further the indentation position was from the middle point (Subsection 2.4.3). Hence, these components were included in the analysis alongside the z-direction force component.

The load displacement curves comparison for the middle and blue point revealed distinct behaviors. For the middle point in Figure 5.10, the x-force component in the computational model was close to zero, in comparison to the experimental data, which possessed a small but noticeable peak. Moreover, the simulation results for this force component appeared unstable.

On the contrary, the y-force component showed a clear nonlinear trend in the computational model, whereas the experimental curve showed minimal variation. The z-force component was previously analyzed and used to identify the material parameters, therefore has the closest match between the curves.

The total force curve exhibited a similar initial slope difference as showcased for the z-force component. However, after reaching a displacement of $u \approx 1.2$ mm, the simulation curve showed an increased slope, diverging slightly from the experimental data.

The calculated NRMSE for all components and the total force reaction of the middle point test were listed in Table 5.5. In the table was observed that the components for x and y showed high NRMSE values, but the z-component and the total force still lied below or slightly higher than the acceptable NRMSE limit of 0.1668.

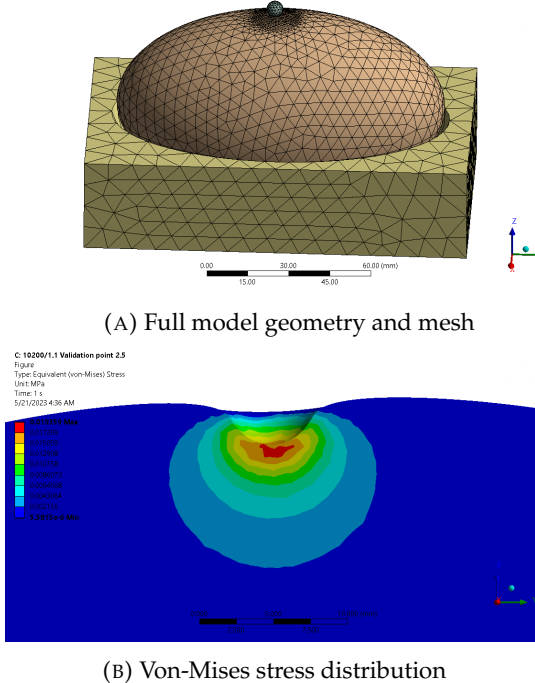


FIGURE 5.9: Blue point computational model with use of the full geometry and stress distribution analysis.

Case	Force	NRMSE
Middle Point	x-component	1.1329
	y-component	67.984
	z-component	0.0534
	Total	0.1669
Blue point	x-component	0.1281
	y-component	1.5615
	z-component	0.0990
	Total	0.1015

TABLE 5.5: Comparison of the NRMSE of all force components and total force reaction for the middle and blue point cases.

The blue point case showed greater alignment across for the x and y-components and the total force reaction, but the NRMSE value for the z-component worsened from 0.0534 to 0.09 (Table 5.5). In this validation case, the force components showed non-linear trends in both the experimental and computational curves, with the simulation closely matching the maximum forces obtained experimentally, with exception of the y-component, as illustrated in Figure 5.11. This indicated that the identified parameters in set 3 was suitable for the blue case as well, in addition to display more stable results for all load-displacements curves.

In conclusion, the third validation case reinforced the validity of set number 3 as the chosen parameter set for this study. This set demonstrated an acceptable level of agreement for all cases with an equal indentation depth. Moreover, this validation supported that this material model can model the behavior of the polyurethane specimen under indentation, particularly when considering different locations on the specimen's surface and all force components into the analysis.

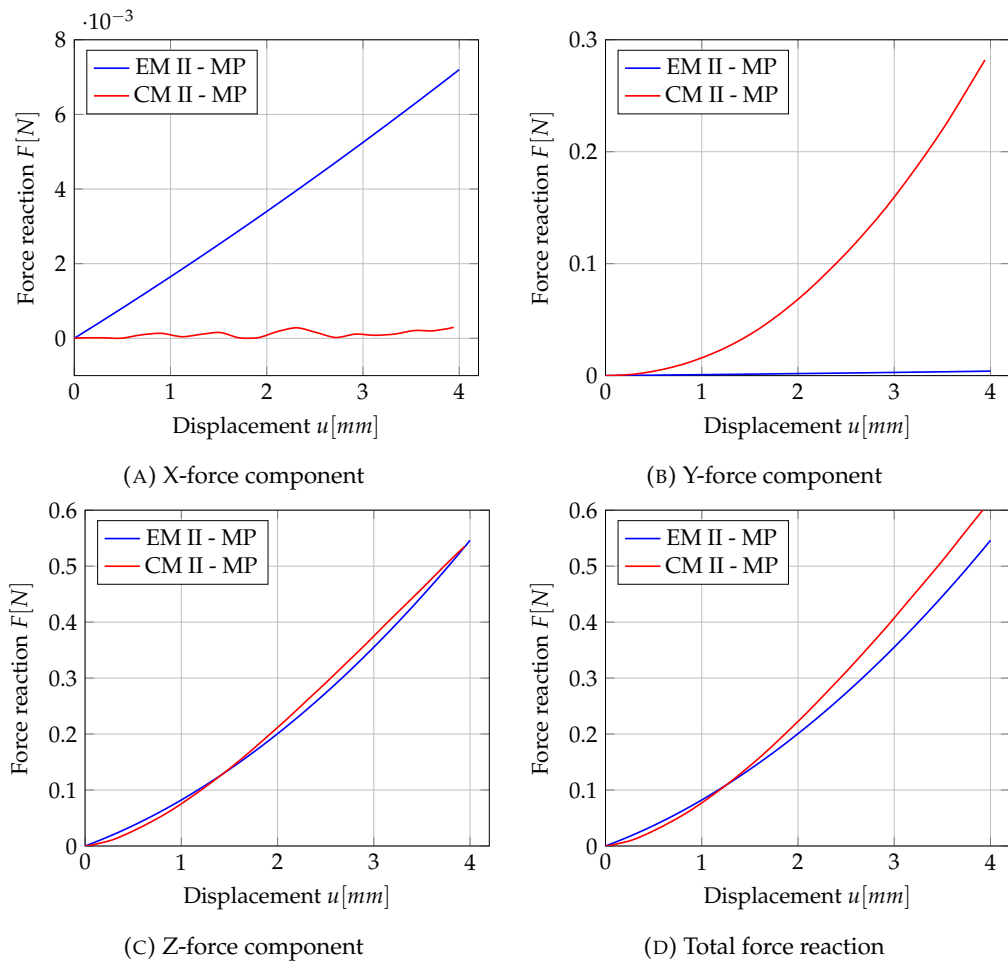


FIGURE 5.10: Middle Point: Comparison and analysis of force components of the experimental data and the computational model.

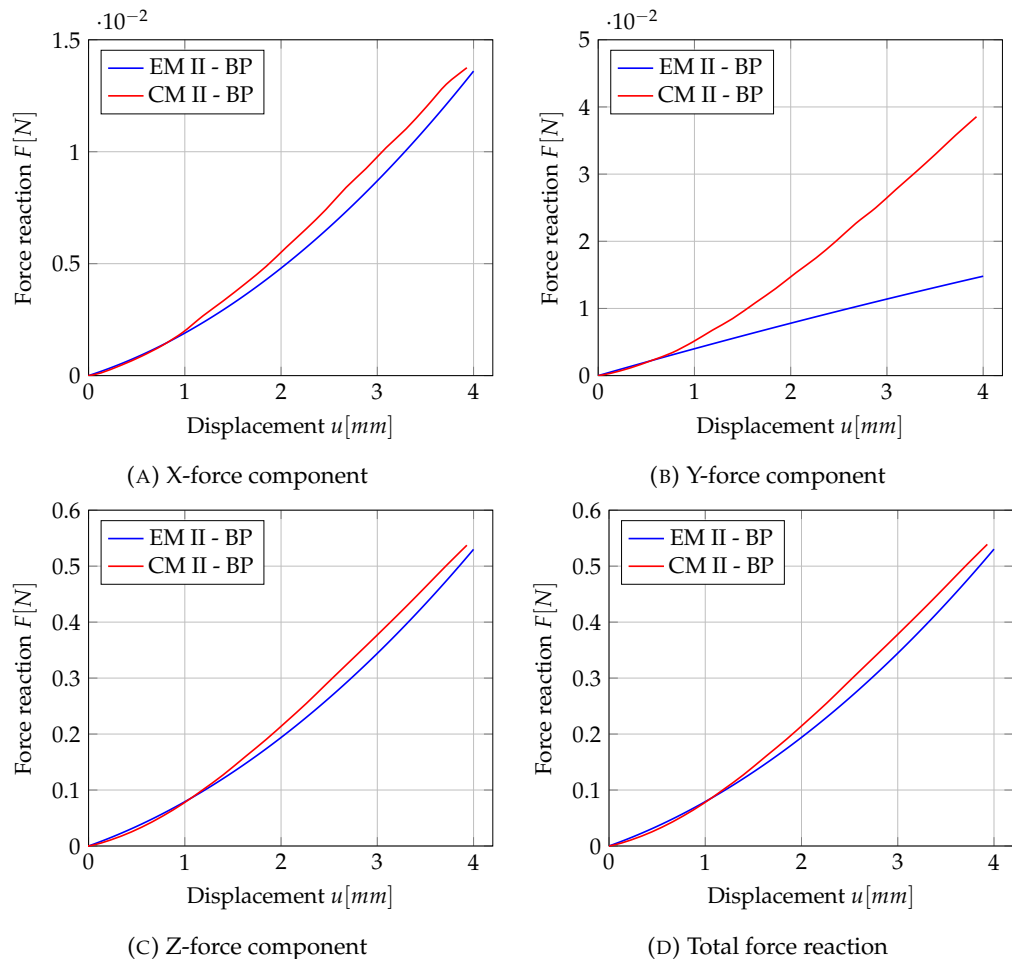


FIGURE 5.11: Blue Point: Comparison and analysis of force components of the experimental data and the computational model.

5.3 Framework Proposal

With this study a framework for the identification of soft material's parameters, focusing on the simplest possible material model was proposed. This framework, illustrated in Figure 5.12, was based on an iFEM approach and provided a robust and systematic procedure that aligns experimental load-displacement data with computational models.

This process began with defining the use case and proceeded with the inclusion of two primary paths running in parallel; the design of the experimental model or comparator, and the computational or FE model.

On the experimental design side, the physical indentation experiments were design and performed (Experimental Model I and II). During these experiments, the mechanical behavior of the material was observed and analyzed. This analysis played a crucial role in establishing the main assumptions for the material model. Furthermore, load-displacement data was captured, which served as the benchmark against which the computational model was verified.

On the computational model design side, the corresponding simulation was constructed to meet the experimental conditions. Here, the simplest material law was selected and initial parameters were set, allowing for the simulation of the indentation process and generation of load-displacement data.

The simulation load-displacement data was then compared with the measured data from the experiments. An important inquiry at this stage was whether the selected material law adequately capture the mechanical behavior of the material. If the answer was no, the material law was adjusted to the next level, and the simulation was rerun. This loop continued until a satisfactory agreement was found.

Once the simulation captured the mechanical behavior, the material parameters' or design parameters were inputted into a response surface optimization process. Here, the definition of an adequate range, played an important role in the obtained candidate sets.

The next step, involved running the simulations for the different candidate points or material parameter sets, and calculating their pre-established error metric. This error metric, such as NRMSE, was used to determine whether these simulations met or surpassed the established error threshold. If the simulation did not meet the threshold, the process was repeated with new sets of candidate material sets.

Finally, once a parameter set met the error threshold, it was identified as the optimal material parameter set. This was an iterative and comprehensive process that ensured that the identified material parameters were not only theoretically robust but also practically validated. This proposed framework is a tool for the identification of material parameters to describe a complex material behavior, representing a balance between simplicity and accuracy.

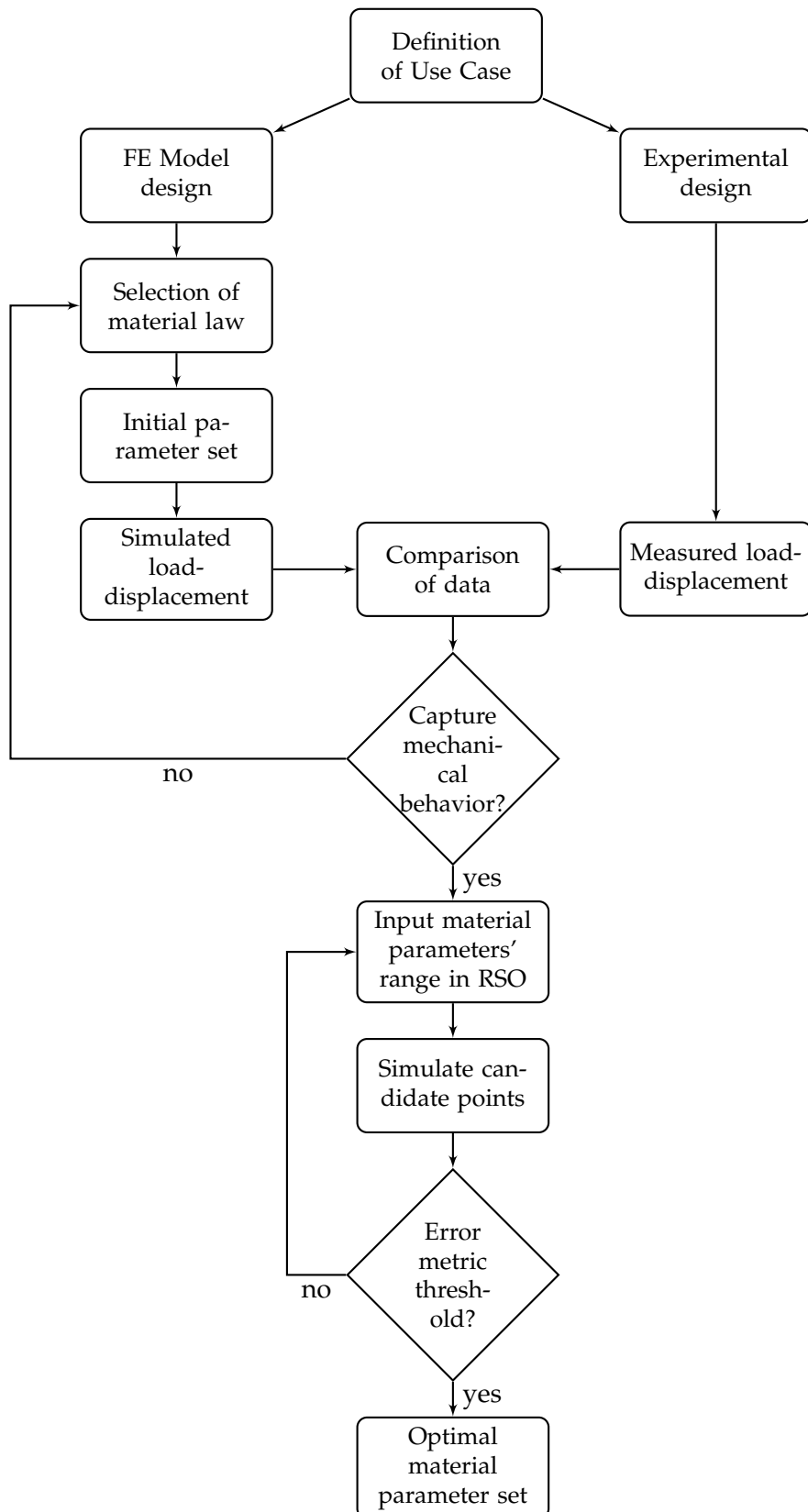


FIGURE 5.12: Flowchart of the identification of soft material parameters based on an iFEM approach conducted in this study.

5.4 Limitations and Implications of the Results

The findings from this study offered valuable insights for the identification of soft material parameters. However, it is essential to acknowledge the limitations of the proposed framework and the obtained results, as well as their implications on its applicability.

One notable limitation arose from the indentation depth used for the identification process. As the indentation depth increased, the accuracy of the material model decreased significantly. Additionally, maintaining the stability of the computational model became increasingly difficult with a larger indentation due to element large deformation issues. This issue was addressed using the nonlinear adaptive meshing option, although it added another layer of complexity to the FE modeling process.

The proposed method demonstrated positive performance for simple testing scenarios, such as vertical indentation and small deformations. As the complexity of the use case increased, the challenge of finding a simple material model capable of accurately replicating the material behavior became more pronounced.

An additional limitation was discovered in the analysis of the deformation profile. It was observed that the Neo-Hookean model could match the experimental deformation profile at a single point but failed to reproduce the entire measured deformation shape. This indicated that a refinement in the experimental procedure, or the selection of a different material model may be necessary to improve the results.

Assumptions made in this study also contributed to certain limitations. The assumed symmetrical deformation might not be applicable to all materials, thereby constraining the framework's utility. Furthermore, the choice of the middle point for the experimental model was based on simplicity and avoid external factor that could influence in the selection of the material model. Nonetheless, this point was not optimal to accurately capturing all force reaction components.

The material parameters' range used in the RSO process affected the obtained candidate points, demonstrating a sensitivity to defined ranges. Noticeably, the best material parameter set found originated from the approximated polynomial global minimum obtained from the MATLAB code, suggesting the potential for further optimization of the range inputted in the RSO process. Despite this, set 1, the best candidate from the RSO process, demonstrated comparable results to the MATLAB set, reinforcing the validity of the proposed methodology.

Lastly, this study highlighted the significance of balancing simplicity and accuracy in material parameter identification process for ultra-soft polyurethane. While the proposed methodology effectively handled simpler cases, the results indicated the need for a more sophisticated approach when dealing with complex deformation scenarios. These findings can provide useful insights and a valuable foundation for further refinement and improvement of parameter identification methodologies.

6 Conclusion and Outlook

6.1 Summary and Contributions

6.2 Recommendations for Future Research

6.3 Conclusions and Final Remarks

A Appendix

A.1 Experimental Research from YNU

Background of Research

In recent years, laparoscopic surgery and robot-assisted surgery, which are less invasive than conventional open surgery, have become popular. Laparoscopic surgery is performed by making multiple 1 cm holes in the abdomen, inserting endoscopes and surgical forceps into the holes, and displaying the intra-abdominal conditions obtained through the endoscopes on a monitor. Laparoscopic surgery has a narrower field of view and provides less information than open surgery, making it difficult to master the technique. For this reason, surgical simulators for preoperative training have been developed to improve physicians' skills. The simulator is given the shape data and physical properties of organs obtained from CT scan data in advance. The position and posture of the surgical instruments are input by moving the instruments attached to the simulator, and the deformed state of the organs and the reaction force to the instruments are calculated as output. The reaction force is transmitted to the haptic device, the surgical tool, as a sensation, and the state of deformation is fed back to the surgeon by being projected on a monitor. In this study, we focus on the physical properties of organs to be input to the simulator. Current simulators use the physical properties of organs that have been processed, tested in vitro, and identified. However, the physical properties of organs in vivo differ from those of organs removed from the body due to cellular transformation and blood flow. Therefore, we believe that the physical property values obtained in in vitro tests may not reproduce the response of organs during surgery. Therefore, the purpose of this study is to identify the physical properties of the whole organ immediately after removal, which is closer to the in vivo state.

Physical Property Identification

Various methods are used to identify physical properties. For example, there are methods that identify the Young's modulus from stress-strain curve obtained from a tensile test, and identify soft tissues by solving an inverse problem based on the results of strain measurement of the tissue using ultrasonic waves. As a method for identifying the physical properties of living organs, the viscoelastic properties of organs are identified by applying vibration to the organs to obtain material property data for use in surgical simulators, and by using the displacement captured by MRI. In this study, a nondestructive indentation test will be employed, which does not involve any treatment that alters the physical properties of the organ, such as damaging. At first, a load is applied to the organ, and the load applied to the organ and the deformation of the organ are measured. And simulate the model of the organ with the same geometry as in the experiment by applying a load to it. If the deformation is out of the acceptable range, the parameters given in the simulation are changed. Then, simulation is performed until the deformation is within the acceptable range, and the parameters obtained when the deformation is within the

acceptable range are used as the physical properties of the organ immediately after removal.

Experimental Requirements

The model is designed to identify the physical properties of organs by performing loading experiments on the organs and inverse analysis of the experimental results using CAE software. Since the internal tissues of organs are complex and the distribution of physical properties may not be uniform, the objective is to improve the accuracy of the model by loading at multiple locations and obtaining results for various deformation modes. Since the inverse analysis uses indentation and reaction forces as inputs, it is necessary to measure them simultaneously. In addition, since the accuracy is expected to be improved by considering the overall deformation as a constraint when determining material parameters in the inverse analysis, the overall deformation is also measured simultaneously. The purpose of this study is to construct a loading system that satisfies the above requirements and to measure the data for the inverse analysis.

Experimental Device

The experimental apparatus is shown in Figure A.1. A Workbee from Ooznest was used as the base actuator for the loading device. The loading device is controlled using G-code, which is used for NC machining. CNCShield for Arduino was used to issue commands to the loading device. In this study, the loading was applied vertically downward to the curved surface of the simulated organ (ellipsoid shape), so a small 6-axis force sensor manufactured by MinebeaMitsumi was used, which can measure reaction forces in directions other than the loading direction. The indentation depth was measured by the trigger voltage using G-code, and the trigger signal was recorded using National Instruments' USB-6003 and DAQ Express software. A spherical measuring element was attached to the tip of the loading rod to prevent breakage. The diameter of the measuring element was 6 mm, and the material was ruby, which has a high level of both rigidity and sphericity. The simulated organs were made of Exseal's human skin gel (ultra-soft urethane resin) and molded into an ellipsoid shape. The deformation of the simulated organ was measured using KEYENCE's IX150 laser displacement meter and WAVE LOGGER X measurement software.

Experimental Procedure

The simulated organ to be loaded is shown in Figure A.2 and a schematic diagram (top view) representing the coordinates of the loading points is shown in Figure A.3. The loading points were set on the dotted line in Figure A.3 because it was considered more suitable for parameter fitting if there were reaction forces of components other than the loading direction when performing the inverse analysis. The loading points were set at the top of the simulated organ and at a total of five points along the dotted line in Figure A.3, moving with increments of $(\Delta X, \Delta Y) = (+2.5 \text{ mm}, +2.5 \text{ mm})$.

The experimental procedure is described below.

1. Set the simulated organ on the table.

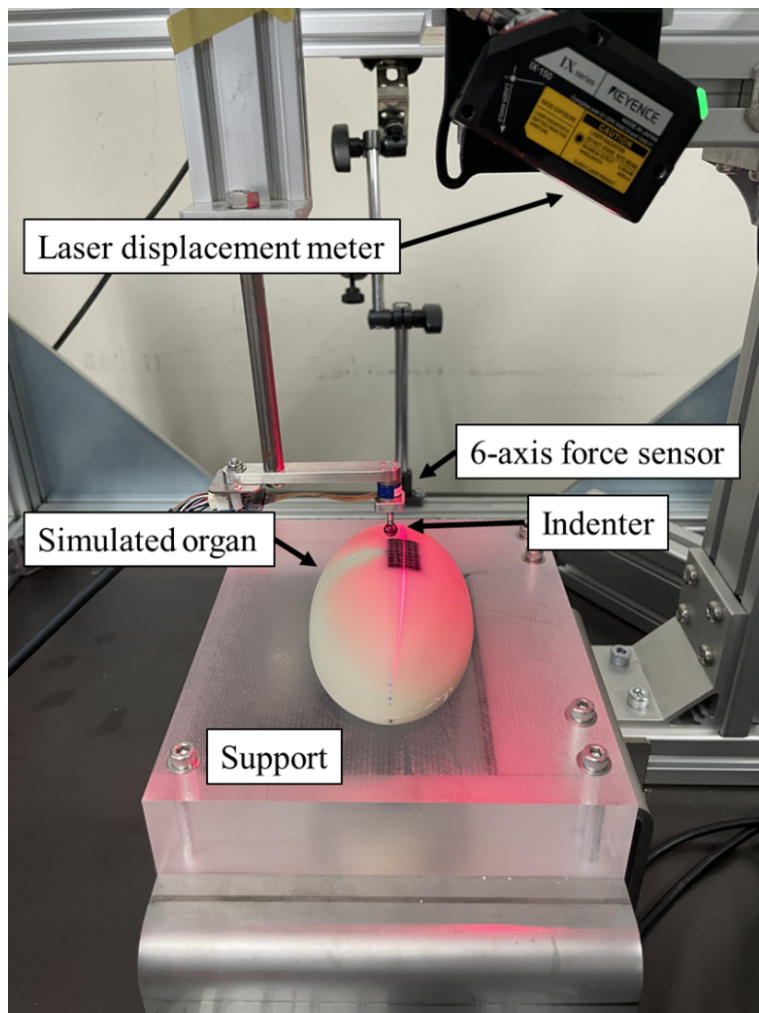


FIGURE A.1: Experimental device

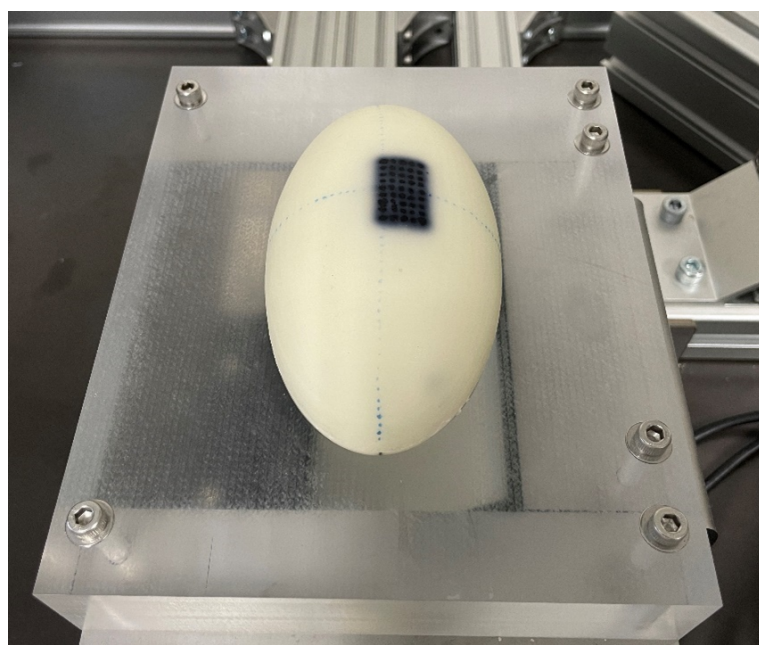


FIGURE A.2: Simulated organ

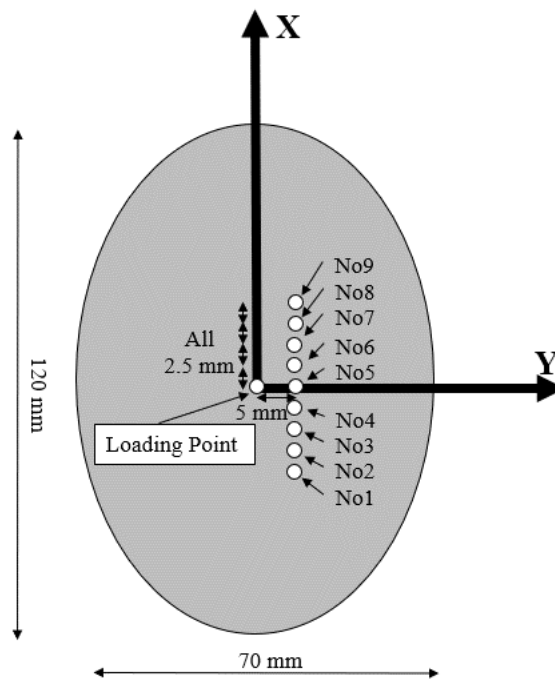


FIGURE A.3: Schematic diagram representing coordinates of loading points (top view)

2. Lubricate the loading point to eliminate the effect of friction.
3. Move the measuring element directly above the loading point.
4. Execute the G-code and start measuring the stroke, reaction force, and deformation.
5. After the G-code is completed, terminate the measurement.
6. Perform the same experiment 5 times for each loading point to confirm reproducibility.

Experiments were conducted under room temperature environment (approx. 20 °C). The loading speed was 30 mm/min, assuming the actual environment.

Measurement method

Measurement of indentation

A 4 mm load was applied to each loading point. The G code used in this study was designed to output a trigger voltage at a total of 81 times, and once when the bar was pushed in 0.1 mm.

These voltage changes were time-stamped using NI's USB-6003 and DAQ Express software. The indentation depth at the time of contact was set to 0 mm, and the amount of indentation depth was measured as 0.1 mm for each time the trigger voltage was transmitted. The sampling frequency was 10 kHz. An example of the voltage change during loading is shown in Figure A.4.

Because the reaction force and voltage were measured independently, the time axis was aligned by matching the peak time of the reaction force in the loading direction and the peak time of the push-in amount (Time when 4 mm indented).

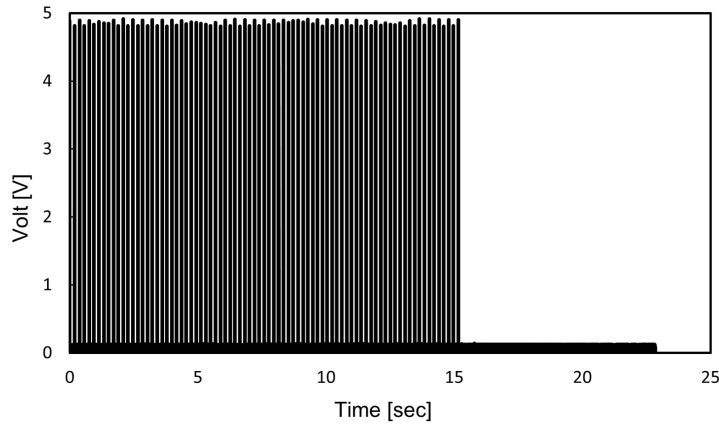


FIGURE A.4: Time history of trigger voltage

Items	Specifications
Size (Outer diameter × height)	φ 9.6mm×9.0mm
Weight	3g
Rated load (force, moment)	40N, 0.4N·m
Load capacity (force, moment)	200N, 1.8N·m
Theoretical resolution (force, moment)	0.001N, 0.00001N·m
Effective resolution (RMS noise) $F_x, F_y / F_z$	0.04N / 0.06N
Effective resolution (RMS noise) $M_x, M_y / M_z$	0.0004N·m / 0.0008N·m
Linearity	± 1.0%FS
Hysteresis	± 1.0%FS
Precision	± 5.0%FS
Interface	SPI
Conversion time	0.78msec
Supply voltage	VDD 3.8V ~14 V VDDIO 1.14V ~ 3.6V

FIGURE A.5: Specifications of miniature 6-axis force sensors

Measurement of reaction forces

The specifications of the compact 6-axis force sensors are shown in Figure A.5. The sampling frequency was 1000 Hz. To reduce the effect of initial drift, we waited five minutes to stabilize after sensor startup.

Measurement of deformation

Figure A.6 shows the laser beam on a straight line. Since the laser displacement meter was run with the same trigger voltage as the stroke measurement, the time when the deformation was measured was based on the time axis of the stroke.

Experimental results

The time history of the reaction force in the loading direction when the top of the simulated organ is loaded is shown in Figure A.7, and the deformation is shown in Figure A.8. We performed five loading experiments to ensure reproducibility. The measurement accuracy of the laser displacement meter is 0.05 mm.

The experimental results show that the deformation of the simulated organ at symmetrically located points, such as measurement points No. 4 and No. 6 (Fig.

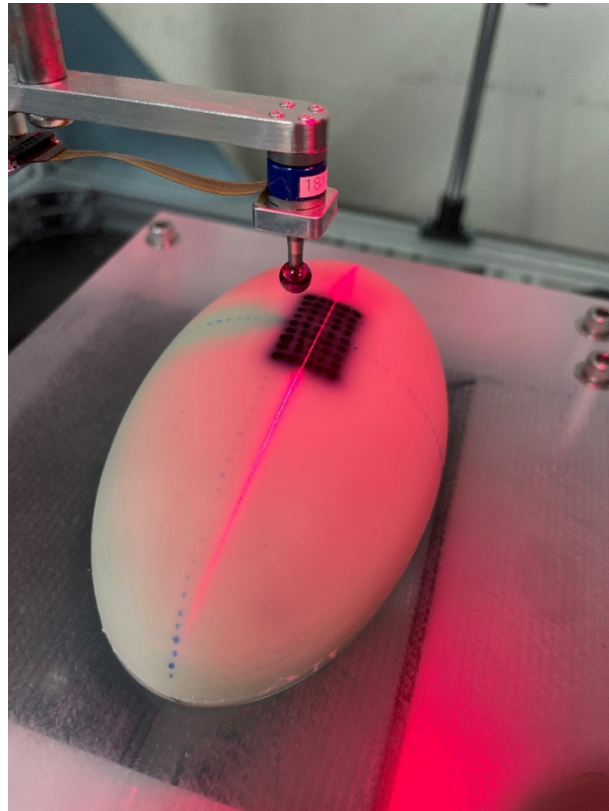


FIGURE A.6: Deformation measurement

A.8b), are in good agreement with the results obtained by the laser displacement meter. The results indicate the possibility of using the deformation state obtained by laser displacement meter for the identification of physical properties in the future.

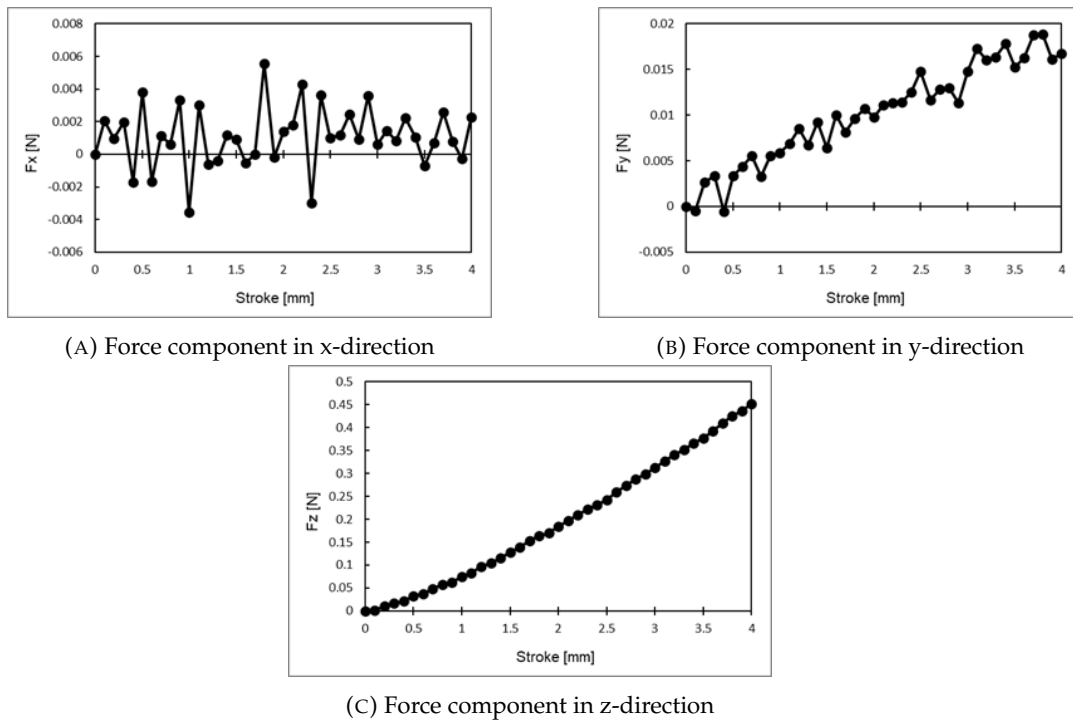


FIGURE A.7: Reaction force components results

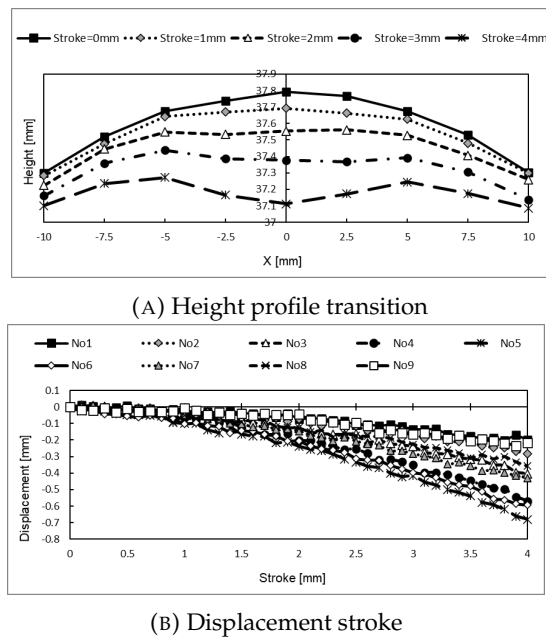


FIGURE A.8: Deformation results

Bibliography

- [1] Nafiseh Ahanchian et al. "Estimating the material properties of heel pad sub-layers using inverse Finite Element Analysis". In: *Medical Engineering and Physics* 40 (2017), pp. 11–19. DOI: 10.1016/j.medengphy.2016.11.003.
- [2] "Ansys Mechanical APDL Element Reference". In: (Nov. 2010).
- [3] Jörgen Bergström. *Mechanics of Solid Polymers: Theory and Computational Modeling*. ISBN: 9780323311502.
- [4] F J Carter et al. *Measurements and modelling of the compliance of human and porcine organs*. 2001, pp. 231–236. URL: www.elsevier.com/locate/media.
- [5] Chen Ket Chai et al. "Local axial compressive mechanical properties of human carotid atherosclerotic plaques-characterisation by indentation test and inverse finite element analysis". In: *Journal of Biomechanics* (2013). DOI: 10.1016/j.jbiomech.2013.03.017.
- [6] A. Chawla, S. Mukherjee, and B. Karthikeyan. "Characterization of human passive muscles for impact loads using genetic algorithm and inverse finite element methods". In: *Biomechanics and Modeling in Mechanobiology* (2009), pp. 67–76. DOI: 10.1007/s10237-008-0121-6.
- [7] Martijn A.J. Cox et al. "Mechanical characterization of anisotropic planar biological soft tissues using large indentation: A computational feasibility study". In: *Journal of Biomechanical Engineering* (3 June 2006), pp. 428–436. DOI: 10.1115/1.2187040.
- [8] Michael Drass et al. "Adhesive connections in glass structures—part I: experiments and analytics on thin structural silicone". In: *Glass Structures and Engineering* 3 (2018). DOI: 10.1007/s40940-017-0046-5.
- [9] Yuan Feng et al. "Characterizing white matter tissue in large strain via asymmetric indentation and inverse finite element modeling". In: *Journal of the Mechanical Behavior of Biomedical Materials* (2017), pp. 490–501. DOI: 10.1016/j.jmbbm.2016.09.020.
- [10] J. Sebastian Giudice et al. "Calibration of a Heterogeneous Brain Model Using a Subject-Specific Inverse Finite Element Approach". In: *Frontiers in Bioengineering and Biotechnology* (2021). DOI: 10.3389/fbioe.2021.664268.
- [11] Amirhossein Goharian, Seyed S.R. Koloor, and Mohamed R. Abdullah. *Biomechanical Evaluation Methods*. Elsevier Inc., 2017, pp. 65–87. DOI: 10.1016/B978-0-12-804634-0.00005-7.
- [12] Gavril Grebenișan and Nazzal Salem. "The multi-objective genetic algorithm optimization, of a superplastic forming process, using ansys". In: *MATEC Web of Conferences* (2017). ISSN: 2261236X. DOI: 10.1051/matecconf/201712603003.
- [13] Michelle Griffin et al. "Biomechanical characterization of human soft tissues using indentation and tensile testing". In: *Journal of Visualized Experiments* (Dec. 2016). DOI: 10.3791/54872.

- [14] Asif Husain, D. K. Sehgal, and R. K. Pandey. "An inverse finite element procedure for the determination of constitutive tensile behavior of materials using miniature specimen". In: *Computational Materials Science* (Sept. 2004), pp. 84–92. DOI: 10.1016/j.commatsci.2004.01.039.
- [15] Mikdam Jamal and Michael N. Morgan. "Characterization of material properties based on inverse finite element modelling". In: 4 (2019). ISSN: 24115134. DOI: 10.3390/inventions4030040.
- [16] J. Joseph et al. "Biomedical applications of polyurethane materials and coatings". In: *Transactions of the Institute of Metal Finishing* (May 2018), pp. 121–129. DOI: 10.1080/00202967.2018.1450209.
- [17] Valentine Kanyanta and Alojz Ivankovic. "Mechanical characterisation of polyurethane elastomer for biomedical applications". In: *Journal of the Mechanical Behavior of Biomedical Materials* 3 (Jan. 2010), pp. 51–62. DOI: 10.1016/j.jmbbm.2009.03.005.
- [18] M. Kauer et al. "Inverse finite element characterization of soft tissues". In: *Medical Image Analysis* 6 (2002), pp. 275–287.
- [19] David C. Lin et al. "Spherical indentation of soft matter beyond the Hertzian regime: Numerical and experimental validation of hyperelastic models". In: *Biomechanics and Modeling in Mechanobiology* (Oct. 2009), pp. 345–358. DOI: 10.1007/s10237-008-0139-9.
- [20] Kaifeng Liu, Mark R. VanLandingham, and Timothy C. Ovaert. "Mechanical characterization of soft viscoelastic gels via indentation and optimization-based inverse finite element analysis". In: *Journal of the Mechanical Behavior of Biomedical Materials* 2 (2009). DOI: 10.1016/j.jmbbm.2008.12.001.
- [21] Yuta Mori. "Development of a method for identifying the physical properties of post-extraction organs". In: (Feb. 2022).
- [22] R.W. Ogden. *Non-Linear Elastic Deformations*. Dover Civil and Mechanical Engineering. Dover Publications, 2013. ISBN: 9780486318714.
- [23] Thomas J. Pence and Kun Gou. "On compressible versions of the incompressible neo-Hookean material". In: *Mathematics and Mechanics of Solids* 20 (2 Feb. 2015), pp. 157–182. ISSN: 17413028. DOI: 10.1177/1081286514544258.
- [24] Rial A. Rajagukguk, Raden A.A. Ramadhan, and Hyun Jin Lee. "A review on deep learning models for forecasting time series data of solar irradiance and photovoltaic power". In: *Energies* (2020). DOI: 10.3390/en13246623.
- [25] Padmanabhan Seshaiyer and Jay D. Humphrey. "A sub-domain inverse finite element characterization of hyperelastic membranes including soft tissues". In: *Journal of Biomechanical Engineering* (3 June 2003). ISSN: 01480731. DOI: 10.1115/1.1574333.
- [26] Lei Shi et al. "Anisotropic Material Characterization of Human Cervix Tissue Based on Indentation and Inverse Finite Element Analysis". In: *Journal of Biomechanical Engineering* (Sept. 2019). DOI: 10.1115/1.4043977.
- [27] Yue Sun et al. "Optimization method for the determination of Mooney-Rivlin material coefficients of the human breasts in-vivo using static and dynamic finite element models". In: *Journal of the Mechanical Behavior of Biomedical Materials* 90 (2019), pp. 615–625. DOI: 10.1016/j.jmbbm.2018.11.016.

- [28] Theodore Sussman and Klaus-Jürgen Bathe. "A finite element formulation for nonlinear incompressible elastic and inelastic analysis". In: *Computers and Structures* (1987), pp. 357–409. DOI: [https://doi.org/10.1016/0045-7949\(87\)90265-3](https://doi.org/10.1016/0045-7949(87)90265-3).
- [29] Wenshou Wang and Chun Wang. *Polyurethane for biomedical applications: A review of recent developments*. Elsevier, 2012, pp. 115–151. DOI: 10.1533/9781908818188. 115.
- [30] Sophie Wendels and Luc Avérous. "Biobased polyurethanes for biomedical applications". In: *Bioactive Materials* (2021). DOI: 10.1016/j.bioactmat.2020.10.002.
- [31] Chen En Wu, Keng Hui Lin, and Jia Yang Juang. "Hertzian load-displacement relation holds for spherical indentation on soft elastic solids undergoing large deformations". In: *Tribology International* (May 2016), pp. 71–76. DOI: 10.1016/j.triboint.2015.12.034.
- [32] George Youssef. *Hyperelastic behavior of polymers*. 2022, pp. 117–144. DOI: 10.1016/b978-0-12-821078-9.00002-8.
- [33] Man Gong Zhang et al. "Spherical indentation method for determining the constitutive parameters of hyperelastic soft materials". In: *Biomechanics and Modeling in Mechanobiology* (1 2014), pp. 1–11. ISSN: 16177959. DOI: 10.1007/s10237-013-0481-4.
- [34] Sylwia D. Łagan and Aneta Liber-Kneć. "Experimental testing and constitutive modeling of the mechanical properties of the swine skin tissue". In: *Acta of Bioengineering and Biomechanics* 19 (2017). DOI: 10.5277/ABB-00755-2016-02.